

**COMPUTATIONAL AND EXPERIMENTAL MODELING OF
SLURRY BUBBLE COLUMN REACTORS**

Grant No. : DE-FG-98FT40117

**US Department of Energy
National Energy Technology Laboratory
University Coal Research
Program Manager: Donald Krastman**

ANNUAL REPORT

Paul Lam, Principal Investigator
Associate Dean, College of Engineering
The University of Akron
Akron, OH 44326-3903
Tel. : 330-972-7230
Email : plam@uakron.edu

and

Dimitri Gidaspow, Co-Principal Investigator
Department of Chemical and Environmental Engineering
Illinois Institute of Technology
Chicago, IL 60616
Tel. : 312-567-3045 Fax : 312-567-8874
Email : gidaspow@iit.edu

September 2000

**COMPUTATIONAL AND EXPERIMENTAL MODELING OF SLURRY
BUBBLE COLUMN REACTORS**

DE-FG-98FT40117

UCR ANNUAL REPORT

Dr. Paul Lam, PI
College of Engineering
The University of Akron
Akron, OH 44326-3903

Tel. : 336-972-7230
Email: plam@uakron.edu

Dr. Dimitri Gidaspow
Dept. of Chemical and
Environmental Engineering
Illinois Institute of Technology
Chicago, IL 60616
Tel. : 312-567-3045, Fax : 312-567-8874
Email: gidaspow@iit.edu

ABSTRACT

The objective of this study was to develop a predictive experimentally verified computational fluid dynamics (CFD) model for gas-liquid-solid flow. A three dimensional transient computer code for the coupled Navier-Stokes equations for each phase was developed. The principal input into the model is the viscosity of the particulate phase which was determined from a measurement of the random kinetic energy of the 800 micron glass beads and a Brookfield viscometer.

The computed time averaged particle velocities and concentrations agree with PIV measurements of velocities and concentrations, obtained using a combination of gamma-ray and X-ray densitometers, in a slurry bubble column, operated in the bubbly-coalesced fluidization regime with continuous flow of water. Both the experiment and the simulation show a down-flow of particles in the center of the column and up-flow near the walls and nearly uniform particle concentration.

Normal and shear Reynolds stresses were constructed from the computed instantaneous particle velocities. The PIV measurement and the simulation produced instantaneous particle velocities. The PIV measurement and the simulation produced similar nearly flat horizontal profiles of turbulent kinetic energy of particles.

This phase of the work was presented at the Chemical Reaction Engineering VIII: Computational Fluid Dynamics, August 6-11, 2000 in Quebec City, Canada. To understand turbulence in risers, measurements were done in the IIT riser with 530 micron glass beads using a PIV technique. The results together with simulations will be presented at the annual meeting of AIChE in November 2000.

OBJECTIVE

This project is a collaborative effort between two universities (The Akron University and Illinois Institute of Technology) and two industries (UOP and Energy International). The overall objective of this research is to develop predictive hydrodynamic models for gas-liquid-solid catalyst reactors using computational fluid dynamics (CFD) techniques. The work plan involves a combination of computational, experimental and theoretical studies with a feedback mechanism to correct models deficiencies. The tasks involve: 1- Development of a CFD code for slurry bubble column reactors; 2- Optimization; 3- Comparison to reactor data; 4- Development of a three dimensional transient CFD code; 5- Measurement of particle turbulent properties; 6a- Measurement of thermal conductivity of particles in the IIT two story riser; 6b- Measurement of evaporation rates of liquid nitrogen in the IIT riser.

ACCOMPLISHMENTS TO DATE

Our paper describing the basic approach using kinetic theory to predict the turbulence of catalyst particles in a slurry bubble column reactor, has been published in a refereed journal (Wu and Gidaspow, "Hydrodynamic simulation of methanol synthesis in gas-liquid slurry bubble column reactors", Chem. Eng. Sci., 55, 2000, pp. 537-587). The computed slurry height, gas hold up and rate of methanol production agreed with the Department of Energy La Porte pilot plant reactor data. The computed turbulent kinetic energy agreed with IIT measurements using a methanol catalyst and with similar measurements at Ohio State University in a bubble column extrapolated to no particles.

We have invented an alternate technique for computing turbulence in a slurry bubble column. It involves direct numerical simulation of the equations of motion with the measured particular viscosity as an input. We have computed the flow profiles, particle concentration profiles and Reynolds stresses for an IIT slurry bubble column. We see good agreement between the computations and the measurements done earlier at IIT. The computations were done using our previous two dimensional three phase code and a newly developed three dimensional version. This work was reported in the Ph.D. thesis by Diana Matonis completed in May 2000 and presented in the CFD conference in Quebec City in August 2000.

Measurements of thermal conductivity of catalyst particles in the IIT riser were completed. They were reported in the last annual report, September 1999. The IIT riser was redesigned to eliminate asymmetries, similarly to Sandia National Laboratory riser, sponsored by the Multiphase Fluid Dynamics Research Consortium. Our CCD camera system was used to measure Reynolds stresses for 530 micron glass beads. We are interpreting the data in terms of effective viscosities as shown in the attached short paper.

Work on the modification of the CFD code to include Fisher-Tropsch kinetics is proceeding cooperatively with The University of Akron.

CFD SIMULATION OF FLOW AND TURBULENCE IN A SLURRY BUBBLE COLUMN

Diana Matonis, Dimitri Gidaspow and Mitra Bahary

**Department of Chemical and Environmental Engineering
Illinois Institute of Technology, Chicago , IL 60616**

ABSTRACT

The objective of this study was to develop a predictive experimentally verified computational fluid dynamic (CFD) model for gas-liquid-solid flow. A three dimensional transient computer code for the coupled Navier-Stokes equations for each phase was developed. The principal input into the model is the viscosity of the particulate phase which was determined from a measurement of the random kinetic energy of the 800 micron glass beads and a Brookfield viscometer.

The computed time averaged particle velocities and concentrations agree with PIV measurements of velocities and concentrations, obtained using a combination of gamma-ray and X-ray densitometers, in a slurry bubble column, operated in the bubbly-coalesced fluidization regime with continuous flow of water. Both the experiment and the simulation show a down-flow of particles in the center of the column and up-flow near the walls and nearly uniform particle concentration.

Normal and shear Reynolds stresses were constructed from the computed instantaneous particle velocities. The PIV measurement and the simulation produced similar nearly flat horizontal profiles of turbulent kinetic energy of particles.

INTRODUCTION

Fluidized beds are widely used industrially because the particles can be introduced into and out of the reactor as a fluid and because of good heat and mass transfer in the reactor. For conversion of synthesis gas into methanol or hydrocarbon liquid fuels, a slurry bubble column reactor has several advantages over a fixed bed reactor (Bechtel Group, 1990; Viking Systems International, 1994). Cooling surface requirement is less than in a fixed bed reactor. Catalyst deactivation due to carbon formation can be handled by catalyst withdrawal and removal, whereas replacement of fixed bed catalyst requires a shutdown. In view of these advantages, slurry bubble column reactors have recently (Parkinson, 1997;) become competitive with fixed bed reactors for converting synthesis gas into liquid fuels. Fan (1989) has reviewed other applications of three-phase fluidization.

Slurry reactor design is usually done (Bechtel Group, 1999; Viking Systems International, 1994) using hold-up correlations. In the early nineties Tarmy and Coulaloglu (1992) of EXXON showed that there were no three phase hydrodynamic models in the literature and that there was a need for such models, as illustrated by the development of a three phase hydrodynamic model at EXXON presented at 1996 Computational Fluid Dynamics in Reaction Engineering Conference (Heard et al., 1996). Today, Computational Fluid Dynamics (CFD) has emerged as a new paradigm for modeling multiphase flow and fluidization, as seen from recent conferences (NICHE, 2000; FLUIDIZATION IX, 1998; CFD in Reaction Engineering, 2000), the formation of an industry-led, Department of Energy Multiphase Fluid Dynamics Research Consortium (Thompson, 1999), which consists of 6 national laboratories, 6 universities and American chemical companies, and papers published throughout the world. The term CFD has come to denote simulation using Navier-Stokes equations.

Three types of CFD models are being used in the literature to model gas-solid multiphase flow and fluidization:

1. Viscosity Input Models, where the principal input is an empirical viscosity. Examples are the papers of Anderson, Sundaresan and Jackson (1995) for bubbling beds, Tsuo and Gidaspow (1990) and Benyahia, Arastoopour and Knowlton (1998) for risers.

2. Kinetic Theory Based Models, as described in Gidaspow (1994).

The most successful example of this model is the prediction of the core-annular regime by Sinclair and Jackson (1989) for steady developed flow in a riser. Transient simulations and comparisons to data were done by Samuelsberg and Hjertager (1996) and Mathiesen, et al (2000) for multisize flow.

3. K-Epsilon Model., where the K corresponds to the granular temperature equation and epsilon is a dissipation for which another conservation law is required. Its success has been to model turbulence for steady single-phase flow. It appears as an option in most commercial CFD codes. Kashiwa and VanderHeyden (1998) are extending this model to multiphase flow as a part of the Multiphase Fluid Dynamics Consortium, where a discussion has begun at the quarterly meetings concerning mechanisms of turbulence production and dissipation.

In single-phase flow, the most fundamental approach to turbulence is DNS, Direct Numerical Simulation of the Navier-Stokes equations. It was quite successful in predicting the logarithmic velocity profile for channel flow (Kim, et al 1985) and other turbulence profiles, but with present computers and solution methods is restricted to relatively low Reynolds numbers, about 10,000. The viscosity input model for multiphase flow is a method similar to the DNS in single phase flow. With particular input viscosities, a system of coupled Navier-Stokes equations is solved producing instantaneous fluctuating velocities. Averaging of these velocities produces the normal and the shear Reynolds stresses for the various phases. Such a computation was recently done for a bubble column by Pan, Dudukovic and Chung (2000) using the Los Alamos CFDLIB code. Their comparison to the Particle Image Velocity (PIV) data of Mudde, et al (1997) was quite good.

This paper presents a similar computation for three phases. The computed time average particle gas and solids hold-ups and the particle velocities generally agree with the measurements in a slurry bubble column. The computed horizontal profile of particle turbulent kinetic energy also agrees with the PIV measurements, similar to those of Mudde, et al (1997).

Recently Pflieger, et al (1999) and Krishna, et al (1999) applied the commercial CFX code to bubble columns using the k-epsilon model, while Grevskott, et al (1996) successfully compared their computed steady state velocity profiles to their experiments. Li, et al (1999) computed the bubble shape in the three-phase system by using an advection equation for the bubble surface. Discrete particle methods have also been used for simulating gas-solid systems (e.g. Xu and Yu, 1997; Kwaguchi, Tanaka and Tsuji, 1998) but have not been applied to slurry bubble columns.

PART I. EXPERIMENTAL BUBBLY COALESCED FLOW REGIME

A. Experimental Setup. The setup used in the bubbly coalesced regime for volume fraction, velocity and viscosity measurement experiments consisted of four major parts: fluidization equipment, densitometers assembly, a high resolution micro-imaging I measuring system or a video-digital camera unit, and a Brookfield viscometer. A schematic diagram of the fluidized bed and video-digital camera unit for velocity measurements is shown in Figure 1. The schematic diagram for source-detector-recorder assembly for X-ray and γ -ray densitometers for volume fraction measurements is shown schematically in Figure 2.

B. Fluidization Equipment. A rectangular bed was constructed from transparent acrylic (Plexiglas) sheets to facilitate visual observation and video recording of the bed operations such as gas bubbling and coalescence, and the mixing and segregation of solids. The bed height was 213.36 cm and cross-section was 30.48 cm by 5.08 cm. A centrifugal pump was connected to the bottom of the bed by a 1.0-inch (2.54 cm) diameter stainless steel pipe. Gas injection nozzles from an air compressor were connected to the sides of the bed. Liquid was stored in and recycled back to a fifty-five gallon storage tank.

The liquid and gas distributors were located at the bottom of the bed. Two perforated Plexiglas plates with many 0.28 cm diameter holes distributed the liquid. They were placed at 35.6 cm and 50.8 cm above the bottom of the bed, with 0.25 cm size glass bead particles filled inside. The gas distributor consisted of six staggered porous tubes of 15.24 cm length and 0.28 cm diameter. The fine pores of porous tubes had mean diameter of 42 μ m. The porous tubes were placed at the bottom of the bed just below the top liquid distributor plate.

C. Densitometer Assembly. Two densitometers were used alternatively for measuring the time-averaged volume fractions of three phases at a designated location by means of the X-ray and γ -ray adsorption techniques. The assembly consisted of radioactive sources as well as detecting and recording devices and a positioning table. A schematic diagram of the source, detector and recording devices assembly is shown in Figure 2.

(1)Radioactive Source. The source is a 200-mCi Cu-244 source having 17.8-year half-life. It emitted X-rays with photon energy between 12 and 23 keV. The source was contained in ceramic enamel, recessed into a stainless steel support with a tungsten alloy packing, and sealed in welded Monel Capsule. The device had brazed Beryllium window. For the γ -ray densitometer, a 20-mCi Cs-137 source having a single γ -ray of 667 keV and a half-life of 30 years was used. The source was sealed in a welded, stainless steel capsule. The source holder was welded, filled with lead, and provided with a shutter to turn off the source. This is the same unit used previously by Seo and Gidaspow (1987).

(2)Detecting and Recording Devices. The intensity of the X-ray beam was measured by using a NaI crystal scintillation detector (Teledyne, ST-82-I/B). It consisted of a 2-mm thick, 5.08 cm diameter tube with 0.13-mm thick Beryllium window. For γ -ray densitometer, the intensity of the γ -ray beam was detected by another NaI crystal detector (Teledyne, S-44-I/2). The dimensions of the crystal were as follows: 5.08 cm thick and 5.08 cm in diameter. The two detectors could be switched for use with different sources. The photomultiplier of the detector was connected sequentially to a preamplifier, an amplifier and a single-channel analyzer, a rate meter, and a 186 IBM compatible personal computer. The rate meter has a selector and a 0-100-mV scale range.

(3)Positioning Table. Both the source holder and detector were affixed to either side of the bed on a movable frame and could be moved anywhere up-or-down or to-and-fro by means of an electric motor.

D. Particle Image Velocity (PIV) System. The digital camera technique used to measure particle velocities as shown on Figure 1 comprised of the following units:

1) Image Recording and Displaying Devices. A high resolution color video camera equipped with electronic shutter speed settings ranging from OFF to 1/10000 sec and super fine pitch color monitor were used to record and display solid velocities.

2) Data Recording Device. A 486 I 33 MHz IBM compatible personal computer with a micro-imaging board inside and a micro-imaging software. Image-Pro Plus were used to record and store raw solid velocities data at any given location inside the fluidized bed.

E. Brookfield Viscometer. Brookfield digital viscometer (model LVDV-II+) with spring a torque of 673.7 dyne-cm was used to measure the effective bed viscosities. This viscometer can produce twenty different rotational speeds ranging from 0 to 100 revolutions per minute (rpm) at four different modes, namely, LV, RV, HA, and HBDVII+.

Experimental Procedure and Interpretation.

A. Fluidization Experiments. The liquid from the storage tank was fed to the bed from the bottom of the bed using the centrifugal pump. The gas was fed to the bed through a compressor. Both gas and liquid from the top of the bed were directed through three openings of 1.0-inch (2.54 cm) diameter back to the storage tank, where the gas was separated from the liquid.

In order to achieve a uniform fluidization, the liquid distributor section was designed in such a way that the pressure drop through the distributor section was 10 - 20 % of the total bed pressure drop. The gas was distributed in the fluidized bed through the six staggered porous tubes.

Air and water were used as the gas and liquid, respectively, in this experiment. Ballotini (leaded glass beads) with an average diameter of 0.8 cm and a density of 2.94 g/cm³ were used as the solids. The experimental operating conditions are shown in the Table 1 (Bahary, 1994).

B. Volume Fractions Determination. X-ray and γ -ray densitometers have been used to measure porosities of fluidized beds (Miller and Gidaspow, 1992; Seo and Gidaspow, 1987; Gidaspow, et al, 1995) and solids concentrations in nonaqueous suspensions (Jayaswal, et al, 1990). These techniques are based on the fact that the liquid, gas and solid phases under consideration have different absorptivities for X-ray and γ -rays. The same concept was adopted to measure concentration profiles inside our three phase fluidization systems.

The intensity of the transmitted X-rays or γ -rays can be described as a linear function of the volume fractions of liquid, gas and the solid phases. The amount of radiation that is absorbed by a material can be given by the Beer-Bougert-Lambert Law:

$$I=I_0\exp (-\kappa \rho l) \tag{1}$$

where I is the intensity of transmitted radiation, I₀ is the intensity of incident radiation, κ is the attenuation coefficient, ρ is the density of material, and l is the path length.

The logarithmic form of equation 1 for three-phase (gas-liquid-solid) fluidized beds is

$$\ln \left[\frac{I}{I_o} \right] = A_g \varepsilon_g + A_l \varepsilon_l + A_s \varepsilon_s \quad (2)$$

where

$$A = \kappa \rho l \quad (3)$$

and where I is the intensity readings of the x-ray or γ -ray densitometers; and ε_g , ε_l and ε_s are the volume fractions of gas, liquid, and solid phases, respectively. The relation for volume fractions is:

$$\varepsilon_g + \varepsilon_l + \varepsilon_s = 1.0 \quad (4)$$

The coefficients in equations (2) were calculated using the least square error technique from the calibration measurements of the intensity readings of X-ray and γ -ray densitometers at known concentrations of gas, liquid and solids in three phase mixtures. However, these coefficients were found to have values with 20% of error for X-ray and 2% of error for γ -ray.

C. Velocity Measurements. In order to get a good visualization of microscopic movement of particles, a fiber-optic light was reflected on the field of view in the front and the back of the bed. The field of view in most experiments was a 2 cm x 2 cm area. As the particles were fluidized inside the bed, the camera with a zoom lens 18-108 mm and close up focus transferred its field of view to the monitor with streak lines. These streak lines represented the space traveled by the particles in a given time interval specified on the camera. The images were then captured and digitized by a micro-imaging board and analyzed using Image-Pro Plus software. Radial and axial velocity measurements were conducted at different locations inside the bed. The velocity vector was calculated as,

$$v_x = \frac{\Delta L}{\Delta t} \cos \alpha \quad (5)$$

$$v_y = \frac{\Delta L}{\Delta t} \sin \alpha \quad (6)$$

where, ΔL is the distance traveled, α is the angle from horizontal, Δt is the inverse of shutter speed, and v_x and v_y are the vertical and horizontal velocity components, respectively.

D. Viscosity Measurements using Brookfield Viscometer. The viscometer was placed at the top of the fluidized bed, and secured over the centerline of the bed. A cylindrical spindle (#1 LV) of 0.9421 cm diameter, 7.493 cm effective length and overall height of 11.50 cm was used. The cylindrical spindle was attached to the bottom of the viscometer without the guard and was lowered inside the fluidized bed by an extension wire until it was completely immersed in the mixture during measurements.

The measurements in this experiment were made under LV mode at different speeds between of 2 and 20 rpm. At each rotational speed, between 10 and 30 readings were taken. The calibration of the viscometer-spindle apparatus was done using a Newtonian liquid, namely, water.

E. Granular Temperature Determination. The granular temperature, which is 3/2 of the random particle kinetic energy, is obtained from the frequency distribution of the instantaneous velocities measured with the PIV system. Figure 4 shows typical distributions. The variances, σ^2 , give the granular temperature, θ , as shown below

$$\theta = \frac{1}{3} [\sigma_x^2 + \sigma_y^2 + \sigma_z^2] \quad (7)$$

Since no distributions were measured into the depth of the bed, the z direction, and since the variance in the direction of flow is the largest, in the calculation the assumption was made that the z direction variance equals the x direction variance. Hence

$$\theta = \frac{1}{3} [2\sigma_x^2 + \sigma_y^2] \quad (8)$$

Experimental Results for Bubbly Coalesced Regime.

A. Phase Hold-Up. From the calibration curves of the x-ray and gamma-ray densitometers, the time average values of volume fraction for liquid, gas and solid phases were calculated. Tables 2 and 3 represent such a subset of the volume fraction of gas and solids at varying heights and two different horizontal positions. The particle and gas concentrations appear to be nearly constant throughout the region. A computer simulation of this system, using the experimental superficial liquid velocity of 2cm/s and gas velocity of 3.37cm/s, also shows uniformity in solids concentration distribution. Figure 3 shows the agreement of the computer simulation with experiment. Computer simulations will be discussed in detail in the next section.

B. Instantaneous Velocity Distribution. The measured velocity data were analyzed using frequency distribution plots. The frequency distribution plots for particles vertical and horizontal velocities are shown in Figures 4(a) and 4(b) for three phase fluidized bed.

C. Granular Temperature. Figures 5 shows a graph of the granular temperature, calculated using particle velocity measurements, as a function of horizontal distance from centerline of the bed at two different heights. The granular temperature of the 800 micron beads is about $100(\text{cm/s})^2$, except near the left wall, where there is a higher velocity and more dilute flow due to the asymmetry in the system. This compares to about $1000 (\text{cm/s})^2$ for 500 micron beads in air, determined in the IIT CFB and about $10 (\text{cm/s})^2$ for 500 micron beads in water measured at IIT. Clearly the gas flow increased the turbulence of the system. For 45 micron methanol catalyst particles, Wu and Gidaspw(2000) computed the granular temperature to be between 20 and 10 for volume fractions corresponding to 0.1 and 0.25, respectively. These computations approximately agree with the measurements of Mostofi

(2000). The lower value of the granular temperature is due to the smaller particle size.

- D. **Fluid Bed Viscosity.** The viscosity of the glass beads in the mixture was obtained in two ways: 1. from a direct measurement of the viscosity by a Brookfield viscometer and 2. from the measurement of the random particle velocity using the equation

$$\mu_s = \frac{5\rho_s d_s (\pi\theta)^{\frac{1}{2}}}{48(1+e)g_o} \left[1 + \frac{4}{5}(1+e)g_o \varepsilon_s \right]^2 + \frac{4}{5}(1+e)g_o \varepsilon_s^2 \rho_s d_s \left(\frac{\theta}{\pi} \right)^{\frac{1}{2}} \quad (10)$$

Gidaspow and Huilin (1996) have shown that these two methods give the same value of the viscosity for 75 micron FCC particles in a riser. The same result holds here, since the large viscosity of the 800 micron beads exceeds the viscosity of water and air. Figure 6 shows that the viscosities are the same within experimental error.

Part II. SIMULATION

Hydrodynamic Model

A transient, isothermal, three-dimensional model for multiphase flow was developed. The hydrodynamic model uses the principle of mass conservation and momentum balance for each phase. This approach is similar to that of Soo(1967) for multiphase flow and of Jackson (1985) for fluidization. The equations are similar to Bowen's (1976) balance laws for multi-component mixtures. The principle difference is the appearance of the volume fraction of phase "k" denoted by ε_k . The fluid pressure, P, is in the liquid (continuous) phase.

For gas-solid fluidized beds, Bouillard, et al. (1989) have shown that this set of equations produces essentially the same numerical answers for fluidization as did the earlier conditionally stable model, which has the fluid pressure in both the gas and the solids phases. In this model (hydrodynamic model B), the drag and the stress relations were altered to satisfy Archimedes' buoyancy principle and Darcy's Law, as illustrated by Jayaswal (1991). Note in Table 4, no volume fraction is put into the liquid gravity term, while in the gas/solid momentum balance contains the buoyancy term. This is a generalization of model B for gas-solid systems as discussed by Gidaspow(1994) in section 2.4. For the solid phase P_k , equation 12, consists of the static normal stress and dynamic stress, called the solids pressure, which arises due to the collision of the particles.

This model is unconditionally well-posed, ie, the characteristics are real and distinct for one-dimensional transient flow. It does not require the presence of solid's pressure for stability and well-posedness.

The numerical method is an extension of Harlow and Amsden's(1971) method, which was subsequently used in the K-FIX program (Rivard and Torrey, 1977). The present program was developed from Jayaswal's two-dimensional MICE program (1991); which originated from the K-FIX program (Rivard and Torrey, 1977). To obtain the numerical solution, the non-uniform computational mesh is used in finite-differencing the equations based on the ICE, implicit Eulerian method (Rivard, 1977; Jayaswal, 1991) with appropriate initial and boundary conditions. Stewart and Wedroff (1984) have critically reviewed the ICE algorithm and related staggered mesh conservative schemes. The scalar variables are located at the cell center and the vector variables at the cell

boundaries. The momentum equation is solved using a staggered mesh, while the continuity equation is solved using a donor cell method.

Table 4 shows the continuity and the separate phase momentum equations for three-dimensional transient three-phase flow. There are nine nonlinear-coupled partial differential equations for nine dependent variables. The variables to be computed are the volume fractions, $\varepsilon_{\text{phases-1}}$, the liquid phase pressure P, and the phase horizontal, x-direction, and vertical velocity, y-direction components, u_{phase} and v_{phase} . The gradient of pressure is in the fluid (continuous) phase only. This leads to an unconditionally well-posed problem, as discussed in detail by Gidaspow(1994) and Lyczkowski, et al. (1978).

A value of 10poises times the particle concentration was used throughout the simulations and the value was obtained by fitting the experimental viscosity values for given superficial liquid and gas velocities (Bahary, 1994). The viscous stress terms for the phases are of the Newtonian form as follows

$$[\bar{\tau}_k] = 2 \varepsilon_k \mu_k [\bar{S}_k]; \quad \mu_k = \varepsilon_k 10(\text{poises}) \quad (11)$$

$$[\bar{S}_k] = \frac{1}{2} [\nabla \bar{v}_k + (\nabla \bar{v}_k)^T] - \frac{1}{3} [\nabla \cdot \bar{v}_k \bar{I}]$$

The solids' pressure is calculated by the solids stress modulus using the following equations,

$$\nabla P_k = G(\varepsilon_k) \nabla \varepsilon_k; \quad G(\varepsilon_k) = 10^{-8.686\varepsilon_k + 6.385} \quad (12)$$

As a particle moves through a viscous liquid there exists a resistance of the liquid to the motion of the particle, hence the interphase drag has to be defined. One type is the packed-pressure drop data expressed in the form of a correlation, such as the Ergun equation. For $\varepsilon_k \geq 0.2$

$$\beta_{fk} = \beta_{kf} = 150 \frac{(1 - \varepsilon_f) \varepsilon_k \mu_f}{(\varepsilon_f d_k \psi_k)^2} + 1.75 \frac{\varepsilon_k \rho_f}{\varepsilon} \quad (13a)$$

For $\varepsilon_k < 0.2$, the empirical correlation is based on Stoke's drag coefficient C_d as follows

$$\beta_{fk} = \beta_{kf} = \frac{3}{4} C_D \frac{\varepsilon_k \varepsilon_f^{-2.65} \rho_f}{d_k \psi_k} |\bar{v}_f - \bar{v}_k| \quad (13b)$$

where

$$C_D = \frac{24}{Re_k} [1 + 0.15 Re_k^{0.687}], \text{ for } Re_k < 1000$$

$$C_D = 0.44, \text{ for } Re_k \geq 1000$$

Arastoopour, Lin and Gidaspow (1980) observed that solid-solid momentum transfer is necessary to correctly predict the segregation among particles of different sizes in a pneumatic conveyor. Particle-particle drag equations to describe such interactions have been derived by several researchers: Soo (1967), Nakamura and Capes(1976) and Syamlal (1985). In the present work the drag coefficient is based on kinetic theory (Syamlal, 1985) represented as

$$\beta_{kl} = \frac{\alpha(1+e)\varepsilon_k \rho_k \varepsilon_l \rho_l (d_k + d_l)^2 \left[1 + 3 \left(\frac{\mathcal{S}_{kl}}{\varepsilon_k + \varepsilon_l} \right)^{\frac{1}{3}} \right]}{2\varepsilon_f (\rho_k d_k^3 + \rho_l d_l^3) \left[3 \left(\frac{\mathcal{S}_{kl}}{\varepsilon_k + \varepsilon_l} \right)^{\frac{1}{3}} - 1 \right]} \quad (14)$$

where

$$\mathcal{S}_{kl} = \begin{cases} \left[(\phi_k - \phi_l) + (1-\alpha)(1-\phi_k)\phi_l \right] \left[\phi_k + (1-\phi_l)\phi_k \right] \frac{\chi_k}{\phi_k} + \phi_l & \text{for } \chi_k \leq \frac{\phi_k}{\left[\phi_k + (1-\phi_k)\phi_l \right]} \\ (1-\alpha) \left[\phi_k + (1-\phi_k)\phi_l \right] (1-\chi_k) + \phi_k & \text{for } \chi_k > \frac{\phi_k}{\left[\phi_k + (1-\phi_k)\phi_l \right]} \end{cases} \quad (15)$$

$$\alpha = \sqrt{\frac{d_l}{d_k}} \quad d_k \geq d_l$$

$$\chi_k = \frac{\varepsilon_k}{\varepsilon_k + \varepsilon_f}$$

Here the gas phase is treated as a particulate phase, since it consists primarily of small bubbles. The quantities are time-average as follows

$$\langle v(x, y, z) \rangle = \frac{1}{t_0} \int_t^{t+t_0} v(x, y, z, t) dt$$

After time-averaging the equations of continuity and of motion, additional terms arise in the equation of motion (Bird et al., 1960). These terms are the components of the turbulent momentum flux and are referred to as the Reynolds stresses. The equations used are summarized in Table 5.

Coordinate system and numerical considerations

The solution of the preceding conservation equations depends on the definition of boundary conditions for adequate comparison to experiment. The diameter of the leaded glass beads was 0.889cm with a density of 2.49 g/cm³. The viscosity was an input in all simulations to match experimentally obtained viscosities. A value of 10 times the local solid volume fraction was used throughout these simulations. Several different inlet conditions and grid size variations were prescribed to test the sensitivity of the final flow field solution. Figure 7, Case FB2d3d in Table 6, illustrates the two-dimensional computational domain. The third dimension, to represent the experimental 5.08 cm depth of the bed, is added with a grid size of 1.02 cm. It will be shown that the two-dimensional simulation can properly represent the flow hydrodynamics and be less computer time intensive. The remainder of this section will be to study the effects of

varying grid size, inlet air bubble diameter and void fraction as represented in Table 4. The left side is taken to be the inlet from left wall to centerline of the horizontal, 15 cm.

Three Dimensional High Flow Simulation: FB2d3d

Flow Field and Averaged Velocity Profiles

Figures 8a and 8b show the three-dimensional time-averaged, 16 to 42 seconds, gas and solid volume fraction contour plots along with the time-averaged velocity vectors at the x-y plane of 3 cm from the front wall. Figure 8c shows the solid contour plot with corresponding velocity vectors at a time of 39 seconds in the y-z plane of 17.5 cm from the left wall. The computed flow pattern correctly shows gas up flow in the center region as visually confirmed in the experiment. A video of the experiment and of the simulations shows that the solid fluctuates upward and downward in the center region. Time-averaged velocities show the solid moving downward in the center as illustrated in Figure 8b. Figure 9 reveals that the two-dimensional time-averaged vertical velocities overlap the three-dimensional time-averaged velocity pattern and both agree well with experiment. Figure 10 further illustrates that the solids vertical velocity does not change when going into the bed. Figure 11 further demonstrates the time-averaged water downward vertical velocities in the center region. This down flow in the center produces a rotation or particle vorticity as seen in Figure 8a. Due to the buoyancy air moves up only.

Reynolds Stresses

The stresses are calculated from the velocity vectors directly using equations presented in Table 5. The profiles of Figures 12 and 14 and all cases studied show that the Reynolds stress $\langle u'u' \rangle$ peaks in the center, whereas $\langle v'v' \rangle$ peaks close to the walls in agreement with Muddle, et al., (1997) and Pan, et al., (2000) for gas-liquid flow only. The explanation of the appearance and diagonal vortical movement by Muddle, et al., (1997) causes drastic swings in the vertical velocity close to the wall, where the motion is primarily upward. In the center, the horizontal velocity attains its highest magnitude, contributing the most to the horizontal stresses in the center, but the least by the wall. At the left wall, the vertical Reynolds stress is the highest, thus the granular temperature exhibits this maximum at the wall as shown in Figure 13. From experiment, Figure 5, the same characteristic experimental maximum turbulence is observed closer to the left wall; even at the lower inlet water and air superficial velocities. Figure 14 shows the stresses plotted into the depth at z-y plane of 12 cm from the left wall. The horizontal stress exhibits the characteristic maximum in the center region, but the vertical Reynolds stress is much flatter. This can be attributed to no vortex formation in the third direction.

Two-Dimensional Low Velocity Simulations

Flow Field and Averaged Velocity Profiles

Figure 15 represents the time-averaged, 15 to 44 seconds, solids contour plot and velocity vectors for Case FB5. Figure 16a illustrates the time-averaged solids' contour plot and velocity vectors for Case FB2. The only difference between these two cases is

the inlet air bubble diameter and grid size. From Figures 18 through 20 it will be shown that grid size did not affect the transient behavior of the bed. Figure 15 and 16a show the difference in the bed expansion is due to the increase in bubble diameter. Figures 16b-c illustrate the instantaneous vortex movement from 14 seconds to 15 seconds for Case FB2.

Figure 17 shows the power spectrum of the vertical velocity for Case FB2 at 8cm from left wall and at a bed height of 11 cm. Muddle, et al., (1997) had found a similar low frequency peak and no dominant frequency above 1 Hz and Bahary (1995) has measured similar low frequencies. The time-averaged vertical and horizontal velocities are presented in Figure 18 and agree with the experimental averages, Figure 4, of 2.3 cm/s for the vertical velocity and -4.32cm/s for the horizontal velocity at a Bed Height of 9 cm and Horizontal Position of 7.5 cm from Left Wall. Figures 18, 19, and 20 represent the time-averaged velocities for the remaining cases with an inlet bubble diameter of 0.01cm. The agreement of the time-averaged velocities of Figures 18, 19 and 20 is expected, since the grid size is the only thing that varies between these cases. However, a noticeable difference exists in these Figures and the two preceding Figures, 21 and 22. Figure 21 represents the time-averaged horizontal and vertical particle velocity profiles for a uniform inlet with only an inlet bubble diameter increase. These profiles are much flatter due to the lack of vortical structure production. Figure 22 represents the larger air bubble diameter and not symmetric inlet conditions (Case FB5). This velocity plot is not flat; instead, there exists an increase in the velocity in the half of the bed where more gas is injected.

Reynolds Stresses and Granular Temperature

The normal and shear stresses are calculated directly from the velocity vectors and presented in Table 5. Figures 23, 24 and 25 show how damping of the stresses occurs by an increase in grid size. From Figure 23 to 24, the y-directional grid cell is halved in size from 2.5/4.5 cm to 1 cm. The shape of the curves remains the same, but the stresses are doubled. The same pattern can be seen when going from Figure 25 to 23, where the x-directional grid cell is halved in length and the stresses are double in size. The stresses appear to be linearly proportional to the grid size.

The granular temperature is compared to experiment in Figure 26 and shows general agreement. The damping in the stresses can also be seen in the granular temperature as the mean fluctuation of the velocity decreases so does the granular temperature. Figure 27 represents the granular temperature of the larger inlet bubble diameter (Case FB4) and as the time-averaged velocity profile was flattened, so is the granular temperature. The test for developed flow, as in DNS for single-phase, was performed on the cases. Figure 28 presents the test for developed flow of case FB3. The following equations are used to obtain the curves

$$\int -\frac{dP}{dy} - g \sum_{i=1}^3 (\epsilon_i \rho_i) dx = \text{pressure drop minus weight of bed} \quad (17)$$

$$\langle u'v' \rangle = \sum_{i=1}^3 (\epsilon_i \rho_i) = \text{principal Reynolds Stress}$$

The two expressions are not equal because the u and v velocities, see Figure 19, are of the same order of magnitude due to the vortex formation. The stresses shown in Figure 28 are on the order of magnitude of the solid's pressure, which is approximately equal to

$$P_s = \varepsilon_s \rho_s v_s^2 \quad (18)$$

This value is small as compared to the fluid pressure.

Discussion

Computations of the granular temperature and frequency allow us to speculate concerning vortex size from dimensional analysis and approximate solutions of Navier-Stokes equations for standing waves (Tolstoy, 1973). Characteristic length equals the pseudosonic velocity divided by the major frequency; where the pseudosonic velocity equals the square root of the granular temperature. The granular temperature ranges between 50 and 100 from Figure 26 and major frequency is taken to be 0.3 Hz. Entering these ranges into the equation gives us vortex sizes of 20 and 30 cm. Hence, in our system we expect to have one to two vortices and do not expect any vortices into the depth. Figure 8 shows that there is no vortex in the third dimension. Figure 16 b-d better illustrates the instantaneous single and double vortices generated by the code and also visible seen in experiment. This fluctuating particle vorticity and the flow of the liquid cause the particle concentration to be uniform throughout the bed. That is in contrast to the case of no liquid flow, where there is a vertical density gradient (Wu and Gidaspow, 2000). Such a catalyst distribution is reasonable. It is usually modeled using a sedimentation model (Viking, 1993). In production of gasoline in a FCC riser, there exists a sharp radial catalyst gradient. In view of this undesirable distribution of particles, other designs such as the downer are being considered. Hence, the discovery of a uniform concentration described in this study is of some practical significance. In the future, this model will be explored further. Further, its' principle weakness is in the uncertainty of the bubble size. Figure 15 and 16 show an order of magnitude difference in bed expansion caused by the order of magnitude increase in bubble diameter. Such an effect is reasonable, since the bed expands a lot more for fine particles or bubbles.

Conclusions

1. A transient, three-dimensional computer code for the solutions of the coupled Navier-Stokes equations for gas-liquid-solid flow was developed. The principal input is the particulate viscosity, which was measured with a Brookfield viscometer and a PIV technique.
2. The computed time-averaged particle velocities and concentrations agree with measurements done in the slurry bubble column with continuous flow of liquid in the churn-turbulent regime. The particle velocities were measured using the PIV technique. The concentrations were determined using a combination of gamma-ray and x-ray densitometers. Both the experiment and the simulations show a downflow of particles in the center of the column with upflow near the wall. The situation is unlike the case of no liquid recirculation (Wu and Gidaspow, 2000) where there exist large inhomogeneities of particles in the bed.
3. Computed instantaneous particle velocities were used to construct normal and shear Reynolds stresses, similar to the procedure in DNS for single-

phase flow. The computed horizontal distributions of granular temperature, the turbulent kinetic energy of particles, agreed with measurements done using a PIV technique.

Acknowledgements

This study was partially supported by Department of Energy Grant No. DE-PS26-98FT98200.

Nomenclature

Abbreviation	Term
C_D	drag coefficient
d_k	characteristic particulate phase diameter
e	coefficient of restitution
g	gravity
G	solid compressive stress modulus
g_o	radial distribution function at contact
P	Continuous phase pressure
P_k	Dispersed(particulate) phase pressure
Re_k	Reynolds number for phase k
t	time
u	horizontal velocity, x-direction
v	vertical velocity, y-direction
w	depth velocity, z-direction
Greek Letters	
β_{km}	interphase momentum transfer coefficient between k and m
ε_k	volume fraction of phase k
θ	granular temperature
μ	viscosity
ρ	density
τ_k	stress
ϕ_k	solids' volume fraction at maximum packing
Ψ	particle sphericity

Literature Cited

Anderson, K., S. Sundaresan and R. Jackson, "Instabilities and the Formation of Bubbles in Fluidized Beds," J. Fluid Mech., 303, 327-366(1995).

- Ahmadi, G. and D. Ma, "A Thermodynamical Formulation for Dispersed Multiphase Turbulent Flows-I," *Int. J. of Mutiphase Flow*, 16, 323-340(1990).
- Arastoopour, H., D. Lin and D. Gidaspow, "Hydrodynamic Analysis of Pneumatic Transport of a Mixture of Two Particle Sizes," in "Multiphase Transport," ed. T.N. Veziroglu, Hemisphere Pub. Corp., 4, 1853-1871(1980).
- Bahary, M., "Experimental and Computational Studies of Hydrodynamics in Three-Phase and Two-Phase Fluidized Beds," PhD Thesis, Illinois Institute of Technology, Chicago (1994).
- Bechtel Group, "Slurry Reactor Design Studies. Slurry vs. Fixed Bed Reactors For Fischer-Tropsch and Methanol: Final Report, No. DE91005752, Jun. 1990.
- Benyahia S. , H. Arastoopour, and T. Knowlton, "Prediction of Solid and Gas Flow Behavior in a Riser Using a Computational Multiphase Flow Approach," *Fluidization X, Proceedings of the Ninth Eng. Found. Conf. On Fluidization*, edited by L.-S. Fan and T. Knowlton, New York, (1998).
- Bird, R.B., W.E. Stewart and E.N. Lightfoot, "Transport Phenomena," John Wiley and Sons, (1960).
- Bouillard, J.X. and D. Gidaspow, "Porosity Distribution in a Fluidized Bed with an Immersed Obstacle," *A.I.Ch.E. Journal*, 35, 908-922(1989).
- Bowen, R.M., "Theory of Mixtures," *Continuum Pysics*, Vol. III, editor A.C. Eringen, Academic Press, New York (1976).
- Courant, R., E. Isaacson and M. Rees, "On the Solution of Nonlinear Hyperbolic Differential Equations by Finite Differences," *Comm. in Pure and Applied Mathematics*, 5, 243(1952).
- Crowe, C., M. Sommerfeld, and Y. Tsuji, *Multiphase Flows with Droplets and Particles*, CRC Press, Boston, (1998).
- Fan, L.-S., "Gas-Liquid-Solid Fluidization Engineering," Butterworths, Boston, Mass. (1989).
- Gidaspow, D., "Multiphase Flow and Fluidization: Continuum and Kinetic Theory Descriptions," Academic Press, New York, NY., (1994).
- Gidaspow, D. M. Bahary and Y. Wu, "Hydrodynamic Models for Slurry Bubble Column Reactors," *Proceedings of Coal Liquefaction and Gas Conversion Contractors Review Conference*, PP. 397-401, DOE/PETC, Aug. 1995.
- Gidaspow, D., and L. Huilin, "Collisional Viscosity of FCC Particles in a CFB," *A.I.Ch.E. Journal*, 42, 2503-2510(1996).
- Gidaspow, D., and L. Huilin, "Equation of State and Radial Distribution Functions of FCC Particles in a CFB," *A.I.Ch.E. Journal*, 44, 279-293(1998).
- Grevskott, S. B.h. Sannaes, M.P. Dudukovic, K.W. Hjarbo and H.F. Svendsen, "Liquid Circulation, Bubble Size Distributions and Solid Movement in Two- and Three-Phase Bubble Columns," *Chem. Eng. Sci.*, 51, 1703-1713(1996).
- Harlow, F.H and A. Amsden, "A Numerical Fluid Dynamics Calculation Method for all Flow Speeds," *Jour. of Comp. Physics*, 8, 197-213(1971).
- Heard, W.B. and G.R. Richter, "Numerical Mutiphase, Multicomponent Flow Modeling," *Computational Fluid Dynamics in Chem. Reaction Eng.*, United Eng. Found., San Diego, Ca., (Oct. 13-18,1996).

- Jackson, R., "Hydrodynamic Stability of Fluid-Particle Systems," in Fluidization, edited by J.F. Davidson, R. Cliff and D. Harrison, Academic Press, New York, 47-72(1985).
- Jayaswal, U.K., "Hydrodynamics of Multiphase Flows: Separation, Dissemination and Fluidization," Ph.D. Thesis, Illinois Institute of Technology, Chicago (1991).
- Kashiwa, B.A. and W. B. VanderHeyden, "An Extended K-Epsilon Turbulence Model for Multiphase Flow," Thirteenth U.S. National Congress of Applied Mechanics, University of Florida, Gainesville, Fl., (June 21-26, 1998).
- Kwaguchi, K., T. Tanaka and Y. Tsuji, "Numerical Simulation of Two-dimensional Fluidized Beds using the Discrete Element Method (Comparison between the Two- and Three-Dimensional Models)," Powder Tech., 96, 129-138(1998).
- Kim, John, P. Moin and R. Moser, "Turbulence Statistics in Fully Developed Channel Flow at Low Reynolds Number," J. Fluid Mec. 177, 133-166(1987)
- Krishna, R. M.I. Urseanu, J.M. Van Baten and J. Ellenberger, "Influence of Scale on the Hydrodynamics of Bubble Columns Operating in the Churn-Turbulent Regime: Experiments vs. Eulerian Simulations," Chem. Eng. Sci., 54, 4903-4911(1999).
- Li, Y. J. Zhang and Liang-Shih Fan, "Numerical Simulation of Gas-Liquid-Solid Fluidization Systems using a Combined CFD-VOF-DPM Method: Bubble Wake Behavior," Chem. Eng. Sci., 54, 5101-5107(1999).
- Lyczkowski, R.W., D. Gidaspow, C.w. Solbrig and E.C. Hughes, "Characteristics and Stability Analysis of Transient One-dimensional Two-Phase Flow Equations and their Finite Difference Approximations," Nuclear Science and Eng., 66, 378-396(1978).
- Mathiesen, V., T. Solberg, H. Arastoopour and B. Hjertager, "Experimental and Computational Study of Multiphase Gas/Particle Flow in a CFB Riser," A.I.Ch.E. Journal, 45, 2503-2518 (1998).
- Matonis, D., "Hydrodynamic Simulation of Gas-Liquid-Solid Fluidized Bed," PhD Thesis, Illinois Institute of Technology, Chicago (2000).
- Miller, A. and D. Gidaspow, "Dense, Vertical Gas-Solid Flow in a Pipe," A.I.Ch.E. Journal, 38, 1801-1815 (1992).
- Mostafi, R., PhD Thesis in progress, (2000).
- Mitra-Majumdar, D., B. Farouk and Y.T. Shah, "Hydrodynamic Modeling of Three-phase Flows through a Vertical Column," Chem. Eng. Sci., 52, 4485-4497(1997).
- Muddle, R.F., D.J. Lee, J. Resse and L.-S. Fan, "Role of Coherent Structures on Reynolds Stresses in a 2-D Bubble Column," A.I.Ch.E. Journal, 43, 913-926(1997).
- Nakamura, K. and C.E. Capes, "Vertical Pneumatic Conveying of Binary Particle Mixtures," Fluidization Technology, Vol. II, New York, 1976.
- Neri, A., D. Gidaspow, "Riser Hydrodynamics: Simulation Using Kinetic Theory," A.I.Ch.E. Journal, 46, 52-67(2000).
- Nikitin, N.V, "A Study of the Near-Wall Turbulent Flows via Direct Numerical Simulations," XIXth International Congress of Theoretical and Applied Mechanics, Kyoto Japan, 451(August 25-31,1996).
- NICHE, The Council for Chemical Research New Industrial Chemistry and Eng., "Computational Chemistry and Fluid Dynamics," Marco Island, Florida, June 11-14, 2000.

- Pan, Y., M.P. Dudukovic, M. Chang, "Numerical Investigation of Gas-Driven Flow in 2-D Bubble Columns," *AICHE J.*, 46, 434-448(2000).
- Parkinson, G., "Fischer-Tropsch Comes Back," *Chem. Eng.*, 104, 39-41(1997).
- Pfleger, D., S. Gomes, N. Gilbert, h.-G. Wagner, "Hydrodynamic Simulations of Laboratory Scale Bubble Columns Fundamental Studies of Eulerian-Eulerian Modeling Approach," *Chem. Eng. Sci.*, 54, 5091-5099(1999).
- Prosperetti, A., "Numerical Aspects of the Simmer-11 Code," *Multiphase Process in LMFBR Safety Analysis*, Ispra, Italy, April, 974-224 (1982).
- Rivard, W.C., and M.D. Torrey, "K-FIX: A Computer Program for Transient Two-dimensional, Two-Fluid Flow," *LA-NUREG-6623*, Los Alamos (1977).
- Samuelsberg, A., and B.H. Hjertager, "Computational Modeling of Gas/Particle in a Riser," *A.I.Ch.E. Journal*, 42, 1536-1546(1996).
- Seo, Y. and D. Gidaspow, "An X-ray-gamma-ray of Measurement of Binary Solids Concentrations and Void in Fluidized Beds," *Ind. Eng. Chem. Res.*, 26, 1622-1628 (1987).
- Soo, S.L., "Fluid Dynamics of Multiphase Systems," *Blaisdell Publ. Co.*, Waltham, Ma., (1967).
- Sinclair, J.L. and R. Jackson, "Gas-Particle Flow in a Vertical Pipe with Particle-Particle Interactions," *AICHE J.*, 35, 1473(1989).
- Stewart, H.B. and B. Wendroff, "Two-Phase Flow: Models and Methods," *J. Comput. Phys.*, 56, 363-409 (1984).
- Symal, M. "Multiphase Hydrodynamics of Gas-Solid Flow," *Ph.D. Thesis*, Illinois Institute of Technology, Chicago, Il., (1985).
- Tarmy, B.L. and C.A. Coualoglou, "Alpha-Omega and Beyond Industrial View of Gas/Liquid/Solid Reactor Development," *Chem. Eng. Sci.*, 47, 3231-3246(1992).
- Thompson, T, "The Multiphase Fluid Dynamics Research Consortium." See "Vision 2020 Comes into Focus," *C&EN News*, Aug.9, 1999.
- Tolstoy, I., "Wave Propagation," *New York*, McGraw-Hill (1973).
- Tsuo, Y.P. and D. Gidaspow, "Computations of Flow Patterns in Circulating Fluidized Beds," *A.I.Ch.E. Journal*, 36, 885-896 (1990).
- Tsuji, Y, T. Tanaka and S. Yonemura, "Cluster Patterns in Circulating Fluidized Beds Predicted by Numerical Simulation (Discrete Particle Model versus Two-Fluid Model)," *Powder Technology*, 95, 254-264(1998).
- Vikings System International, "Design of Slurry Reactor for Indirect Liquefaction Applications," *Report to DOE/PETC by A. Prakash and P.B. Bendale*, DE-AC22-89PC89870.
- Wu, Y. and D. Gidaspow, "Hydrodynamic Simulation of Methanol Synthesis in Gas-Liquid Slurry Bubble Column Reactors," *Chem. Eng. Sci.*, 55, 573-587(2000).
- Xu, B.H., A.B. Yu, "Numerical Simulation of the GAS-Solid Flow in a Fluidized Bed by Combinin Discrete Particle Method with Computational Fluid Dynamics," *Chem. Eng. Sci.*, 52,2785- 2809(1997).

TABLE 1. Operating Conditions for Bubbly Coalesced Regime Experiments

Temperature (°C)	23.5
Particle Mean Diameter (cm)	0.8
Particle Density (g/cm ³)	2.94
Initial Bed Height (cm)	22 /24
Minimum Fluidization Velocity (cm/s)	0.76

Table 2. Measured Phase Hold-up in Bubble Coalesced Regime for $V_{\text{gas}}=3.37\text{cm/s}$ at 4 cm from the Horizontal Center.

Bed heights, cm	2.5	5	7.5	10	12.5	15	17.5
ϵ_{solid}	0.25	0.18	0.15	0.16	0.2	0.25	0.2
ϵ_{air}	0.56	0.4	0.34	0.36	0.36	0.3	0.32

Table 3. Measured Phase Hold-up in Bubble Coalesced Regime for $V_{\text{gas}}=3.37\text{cm/s}$ at -13 cm from the Horizontal Center.

Bed heights, cm	2.5	5	7.5	10	12.5	15	17.5
ϵ_{solid}	0.15	0.21	0.08	0.12	0.1	0.15	0.16
ϵ_{air}	0.5	0.43	0.4	0.41	0.35	0.41	0.53

Table 4. Governing Equations

Continuity Equation for Each Phase, k=g,l,s

$$\frac{\partial}{\partial t} (\varepsilon_k \rho_k) + \nabla \cdot (\varepsilon_k \rho_k \bar{\mathbf{v}}_k) = 0$$

Continuous Phase (Liquid) Momentum Balance

$$\begin{aligned} \frac{\partial}{\partial t} (\varepsilon_f \rho_f \bar{\mathbf{v}}_f) + \nabla \cdot (\varepsilon_f \rho_f \bar{\mathbf{v}}_f \bar{\mathbf{v}}_f) = & -\nabla \cdot P \bar{\mathbf{I}} + \rho_f \bar{\mathbf{g}} + \\ & \sum_{m=g,s} \beta_{fm} |\mathbf{v}_m - \mathbf{v}_f| + \nabla \cdot \bar{\boldsymbol{\tau}}_f \end{aligned}$$

Dispersed Phase (Gas or Solid) Momentum Balance

$$\begin{aligned} \frac{\partial}{\partial t} (\varepsilon_k \rho_k \bar{\mathbf{v}}_k) + \nabla \cdot (\varepsilon_k \rho_k \bar{\mathbf{v}}_k \bar{\mathbf{v}}_k) = & -\nabla P_k \bar{\mathbf{I}} + \frac{\varepsilon_k}{\varepsilon_f} \left(\rho_k - \sum_{m=f,g,s} \varepsilon_m \rho_m \right) \bar{\mathbf{g}} + \\ & \sum_{\substack{m=l,g,s \\ m \neq k}} \beta_{fm} |\bar{\mathbf{v}}_m - \bar{\mathbf{v}}_k| + \nabla \cdot \bar{\boldsymbol{\tau}}_k \end{aligned}$$

Viscous Stress Tensor

$$[\bar{\boldsymbol{\tau}}_f] = 2 \varepsilon_k \mu_k [\bar{\mathbf{S}}_f]$$

$$[\bar{\mathbf{S}}_f] = \frac{1}{2} [\nabla \bar{\mathbf{v}}_f + (\nabla \bar{\mathbf{v}}_f)^T] - \frac{1}{3} [\nabla \cdot \bar{\mathbf{v}}_f \bar{\mathbf{I}}]$$

Table 5. Equations of the calculated stresses.

$$\langle v'v' \rangle = \left[\frac{1}{N(t)} \sum v(x, y, z, t)v(x, y, z, t) \right] - (\langle v(x, y, z) \rangle)^2$$

$$\langle u'v' \rangle = \langle v'u' \rangle = \frac{1}{N(t)} \sum \left[\{u(x, y, z, t) - \langle u(x, y, z) \rangle\} \{v(x, y, z, t) - \langle v(x, y, z) \rangle\} \right]$$

$$\langle u'u' \rangle = \left[\frac{1}{N(t)} \sum u(x, y, z, t)u(x, y, z, t) \right] - (\langle u(x, y, z) \rangle)^2$$

$$\langle u'w' \rangle = \langle w'u' \rangle = \frac{1}{N(t)} \sum \left[\{u(x, y, z, t) - \langle u(x, y, z) \rangle\} \{w(x, y, z, t) - \langle w(x, y, z) \rangle\} \right]$$

$$\langle w'w' \rangle = \left[\frac{1}{N(t)} \sum w(x, y, z, t)w(x, y, z, t) \right] - (\langle w(x, y, z) \rangle)^2$$

$$\langle v'w' \rangle = \langle w'v' \rangle = \frac{1}{N(t)} \sum \left[\{v(x, y, z) - \langle v(x, y, z) \rangle\} \{w(x, y, z) - \langle w(x, y, z) \rangle\} \right]$$

with N(t) being the number of vectors in the time-average

Table 6. Simulation Cases under Investigation

Case	$\Delta x, \text{ cm}$	$\Delta y, \text{ cm}$	V_{Liquid} cm/s	V_{Gas} cm/s	$D_{\text{air}},$ cm	$\epsilon_{\text{left, water}}$	$\epsilon_{\text{left, gas}}$	$\epsilon_{\text{right, water}} = \epsilon_{\text{right, gas}}$
FB2d3d	15*2	18*5.825	8.074	6.078	0.1	0.6	0.4	0.5
FB1	32x1cm	2*2.25, 19*4.5	4.04	3.37	0.01	0.5	0.5	0.5
FB2	32x1	31x1, 2,3,4,10x5	4.04	3.37	0.01	0.5	0.5	0.5
FB3	14x2.5	2*2.25, 19*4.5	4.04	3.37	0.01	0.5	0.5	0.5
FB4	14*2.5	2*2.25, 19*4.5	4.04	3.37	0.1	0.5	0.5	0.5
FB5	15*2.03 2	18*5.623	4.04	3.37	0.1	0.6	0.4	0.5

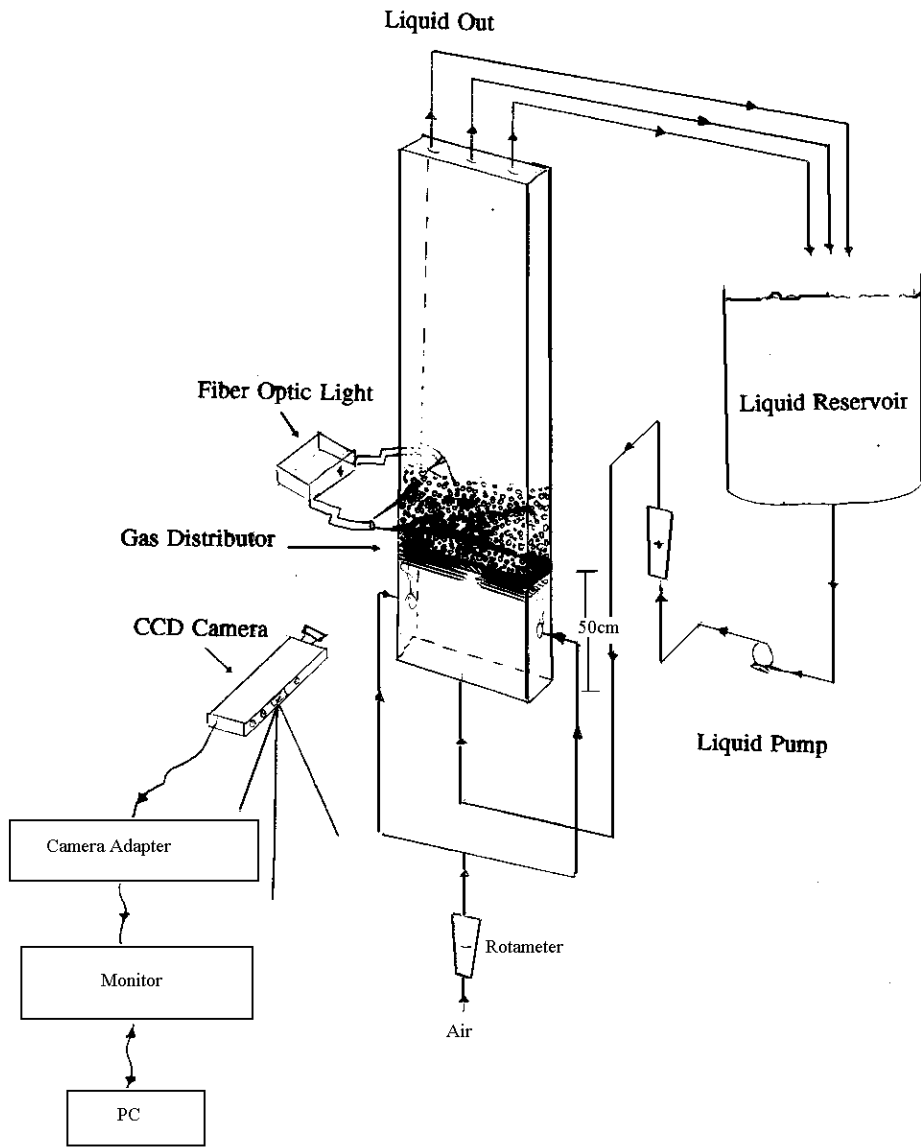


Figure 1. Experimental Schematic Diagram for Three-Phase Fluidization System.

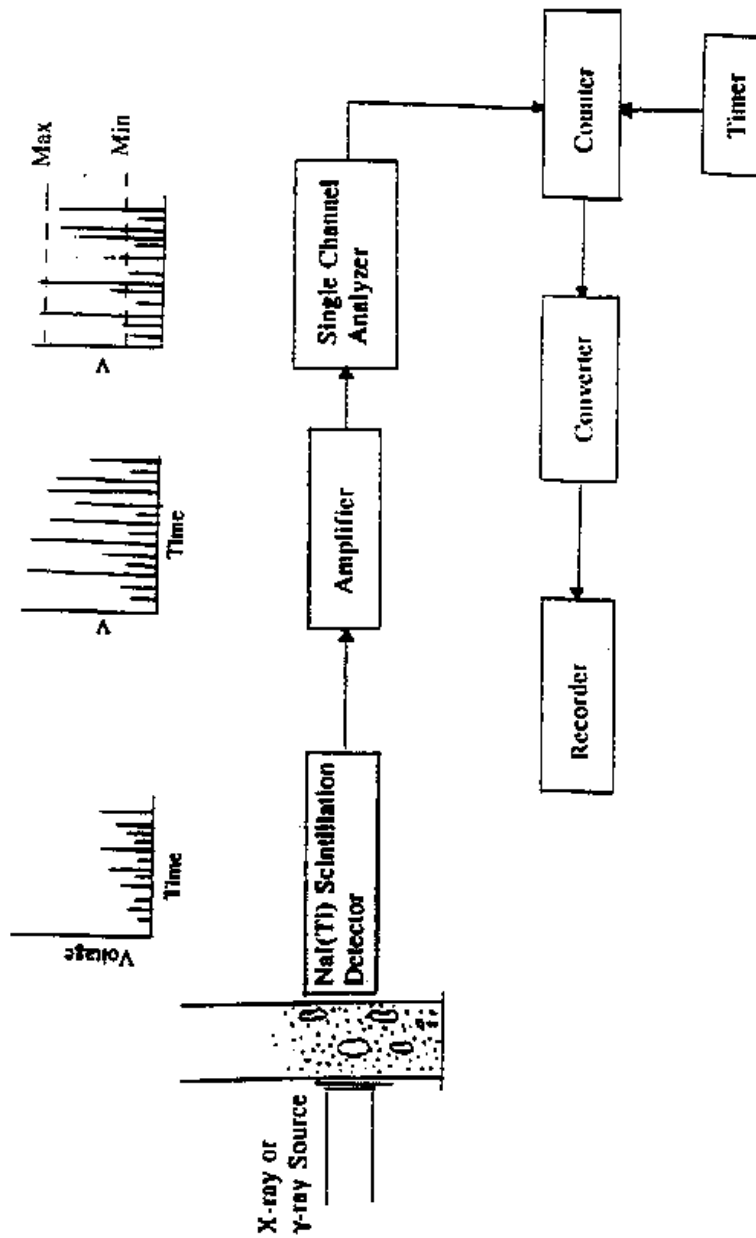
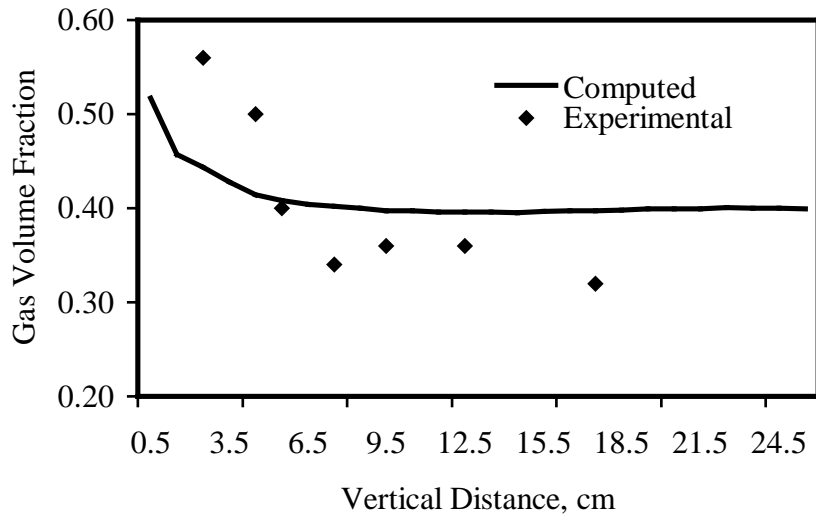
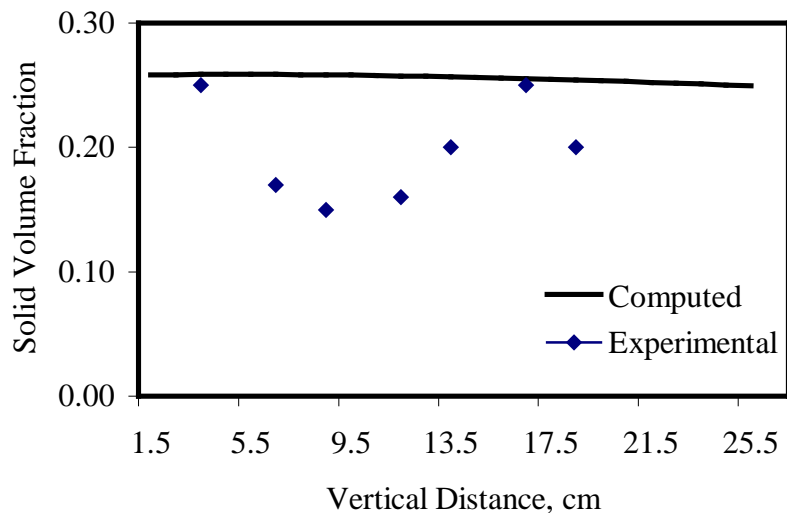


Figure 2. Schematic Diagram for Source-Detector-Recorder Assembly for X-Ray and γ -Ray Densitometers.

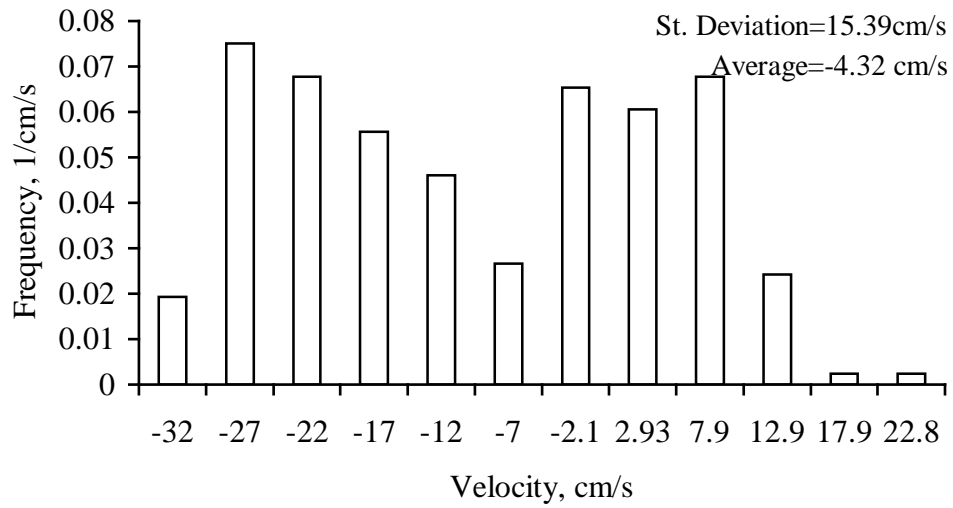


(a)

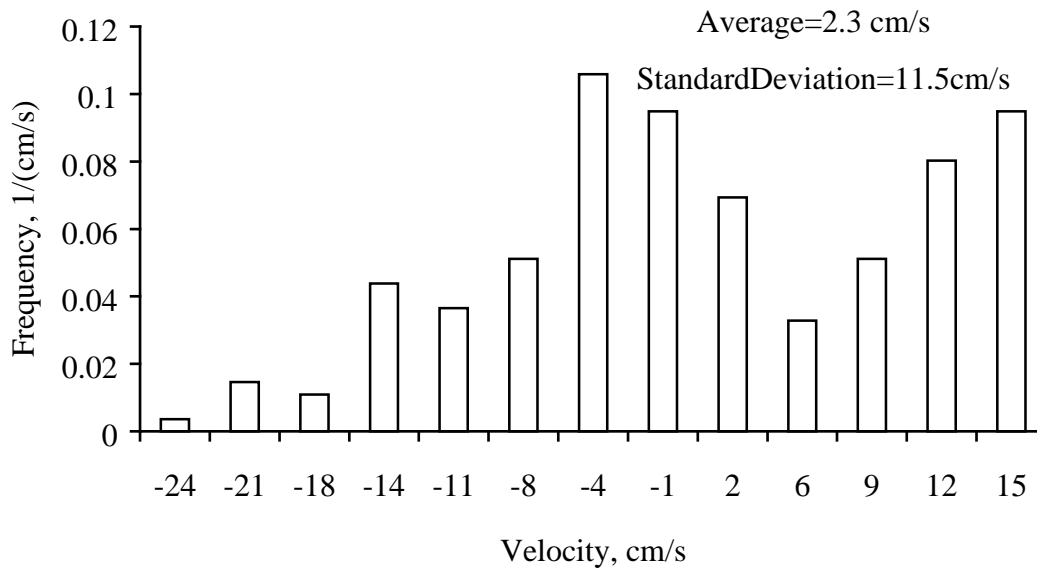


(b)

Figure 3 (a),(b). Comparison of measured and computed phase hold-up in bubbly coalesced regime for $V_L=2.04\text{cm/s}$ and $V_G=3.37\text{cm/s}$ at 4 cm from horizontal center of bed.



(a)



(b)

Figure 4. Experimental Vertical (a) and Horizontal (b) Velocity Distribution of Solids' at a Bed Height of 9 cm and Horizontal Position of 7.5 cm from Left Wall.

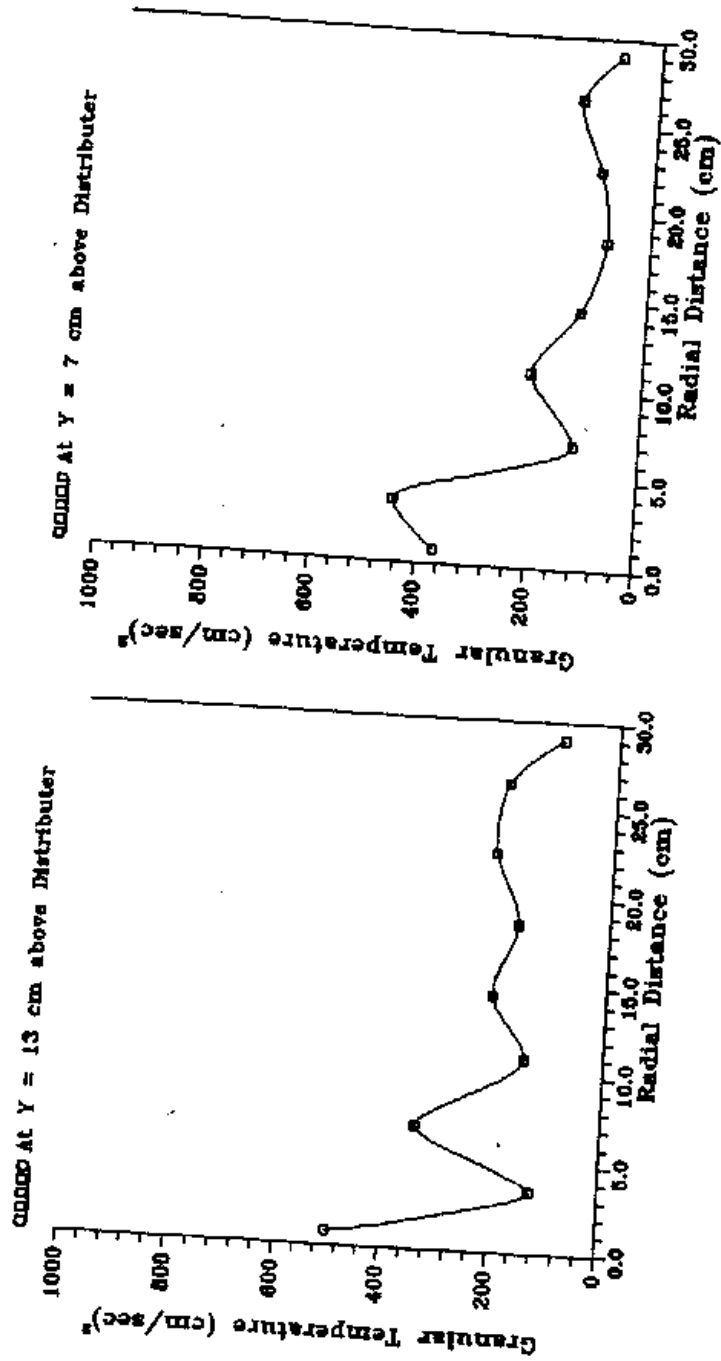


Figure 5. Granular Temperature vs. Radial Distance at Different Bed Heights in Gas-Liquid-Solid Fluidized Bed at Sup. Liquid Velocity of 4.04 cm/sec and Sup. Gas Velocity of 3.36 cm/sec.

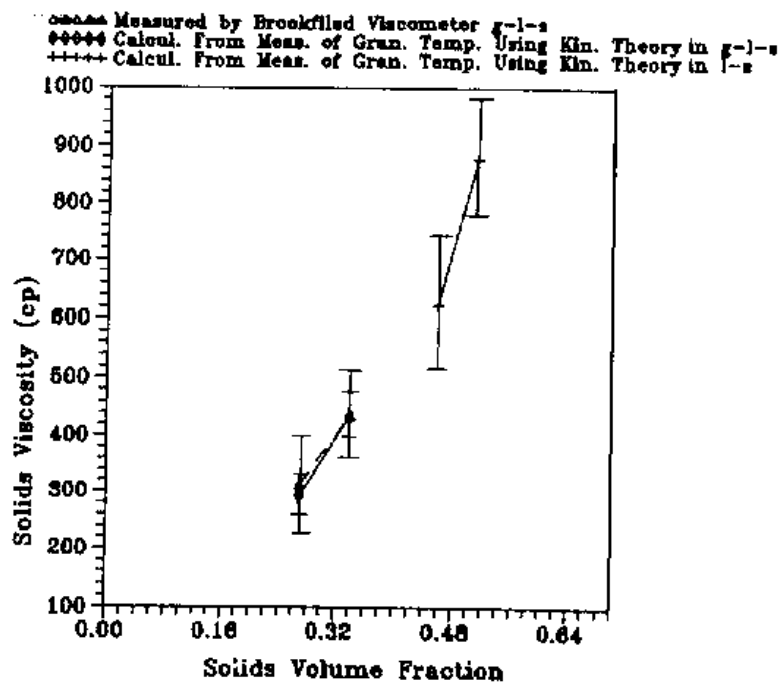


Figure 6. Viscosities determined with a Brookfield Viscometer and from a measurement of random particle oscillations using PIV.

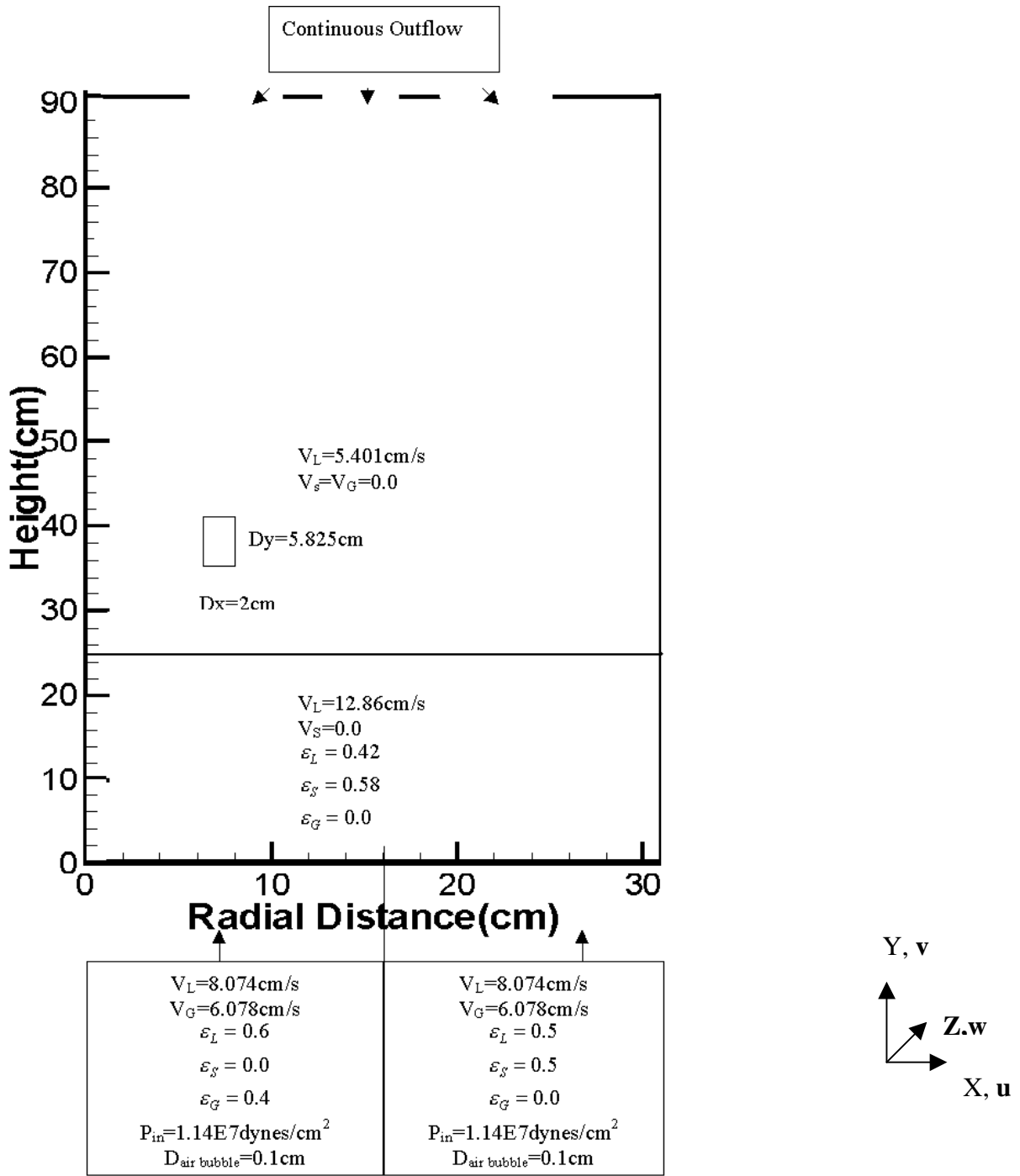
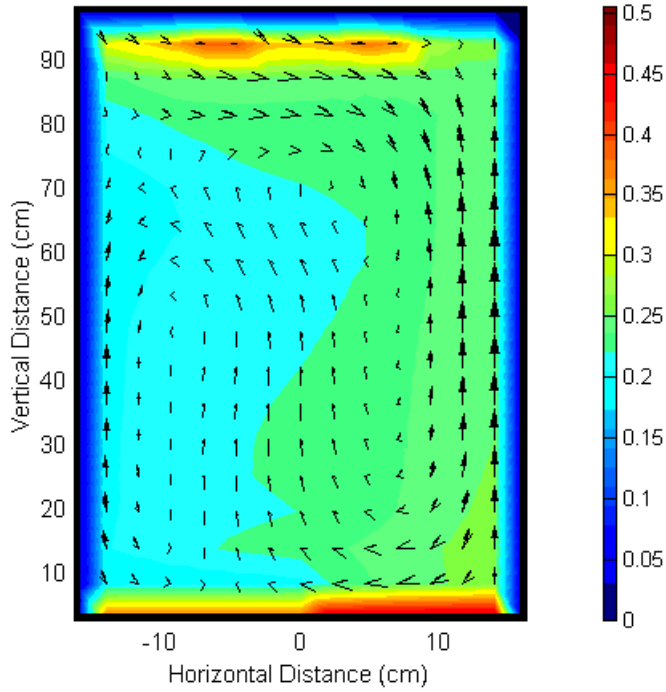


Figure 7. Inlet and initial conditions for simulations.

Velocity Arrow Plot of Gas Averaged from 16 to 42 sec



Velocity Arrow Plot of Solid 2 Averaged from 16 to 42 sec

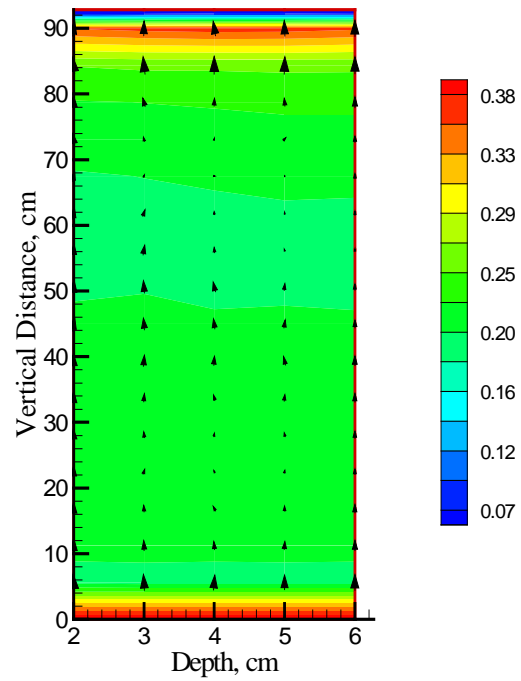
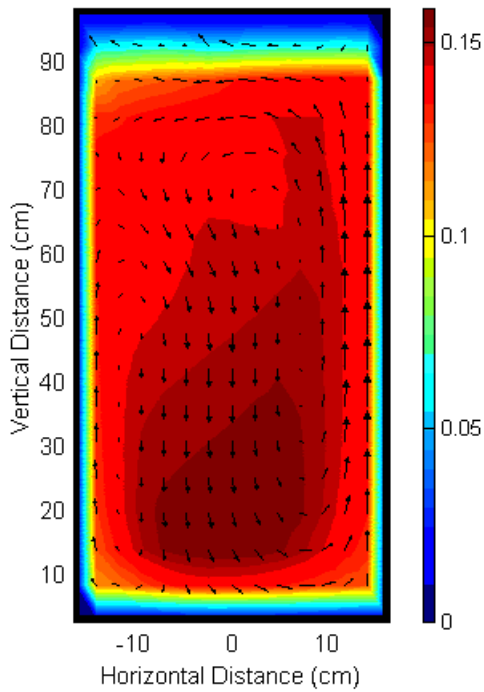


Figure 8. Time-averaged volume fractions and velocities (a)[top,left] for gas, (b)[bottom,center] for particles and 3 cm from front wall (c)[right] for particles.

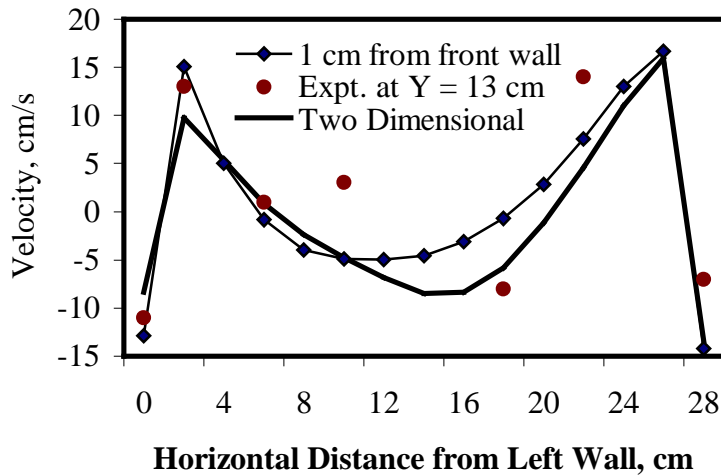


Figure 9. A comparison of two and three-dimensional vertical particle velocities to PIV measurements.

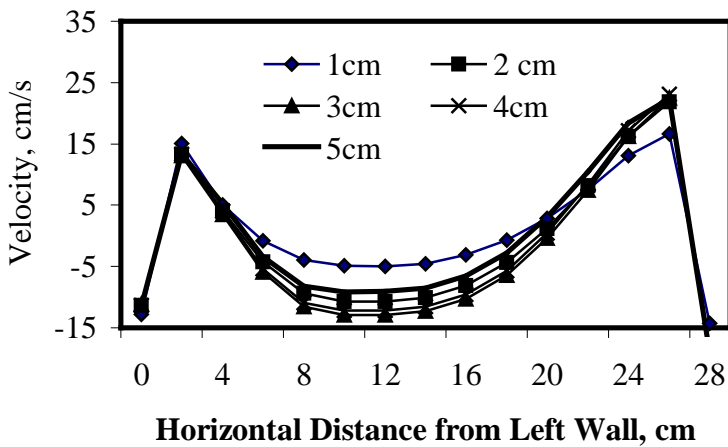


Figure 10. Time-averaged vertical particle velocities for various depths from front plate.

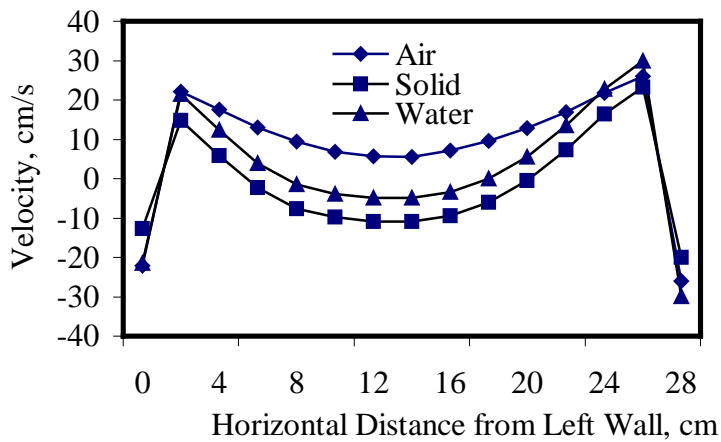


Figure 11. A comparison of the time-averaged vertical velocities for gas, particles and liquid at the center of the vessel.

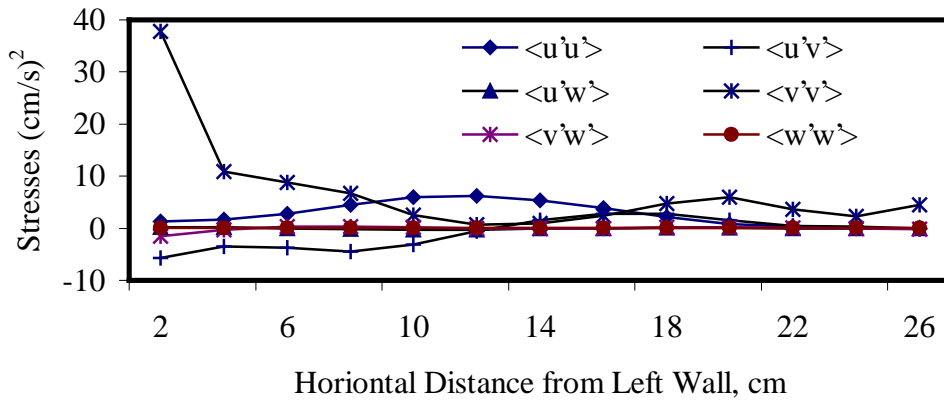


Figure 12. Typical computed Reynolds' stresses for particles at a bed height of 11.3 cm.

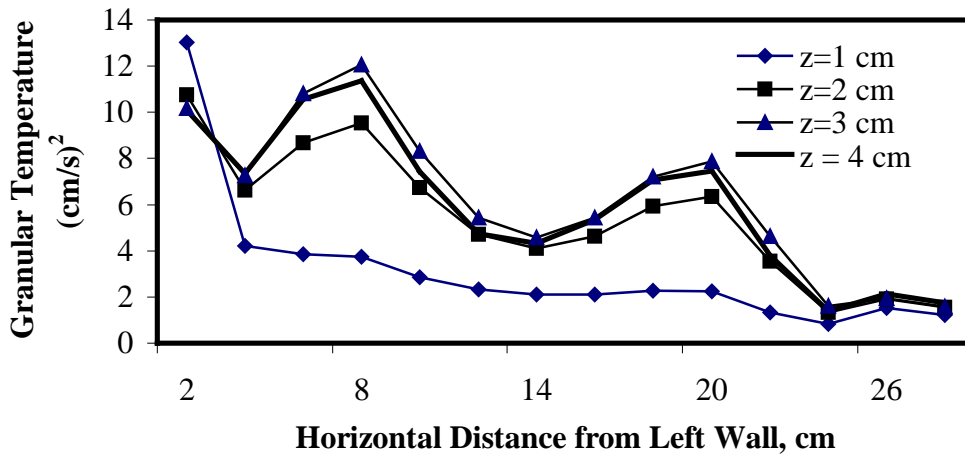


Figure 13. Granular Temperature ($3/2$ particle random kinetic energy) at several bed depths.

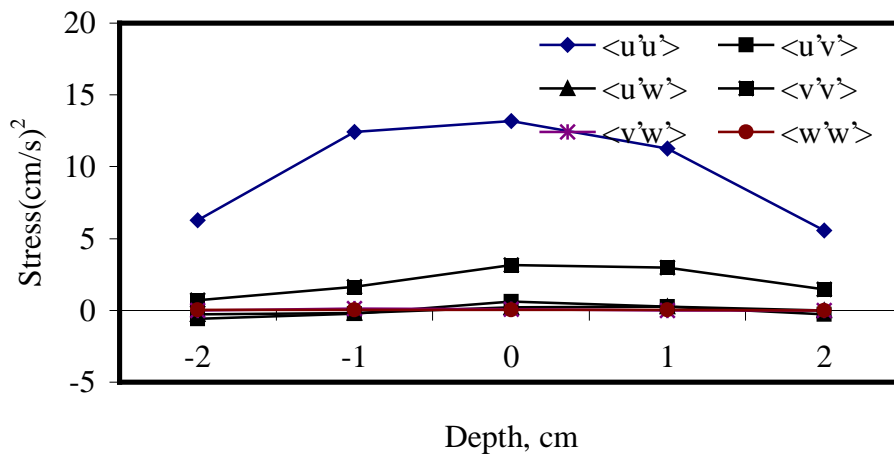


Figure 14. Variation of Reynolds stresses with depth at a bed height of 11.3 cm and 12 cm from Left Wall.

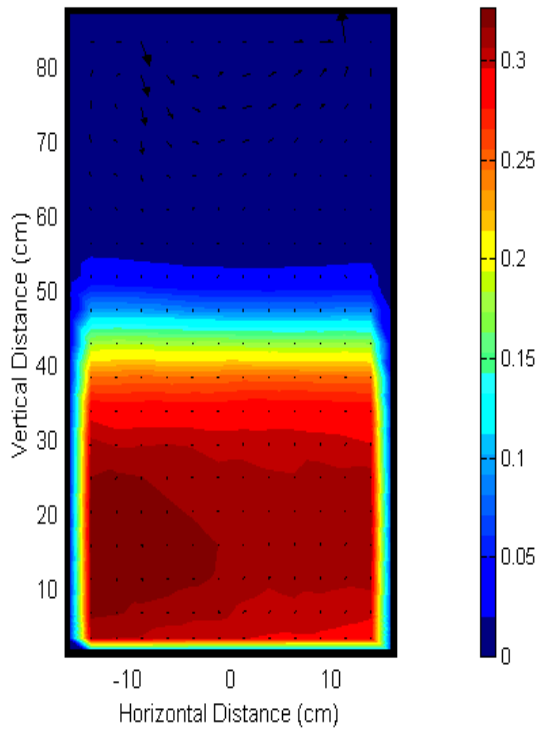


Figure 15. Particle contour and velocity vector plot for Case FB5.

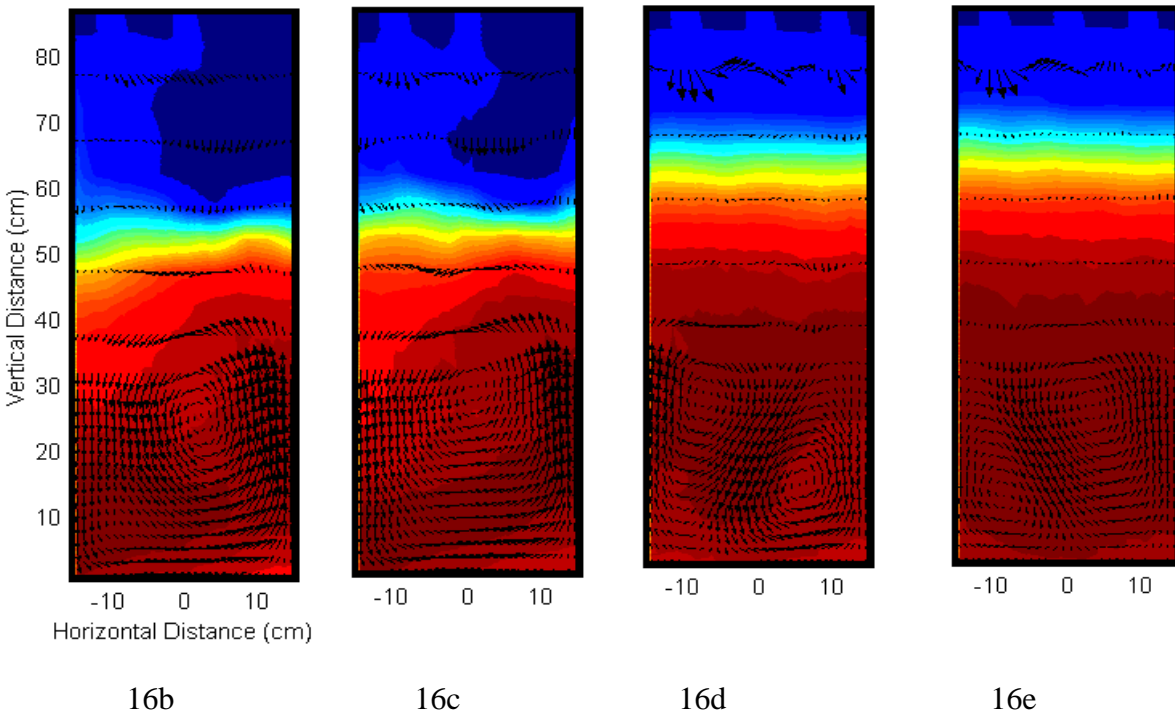
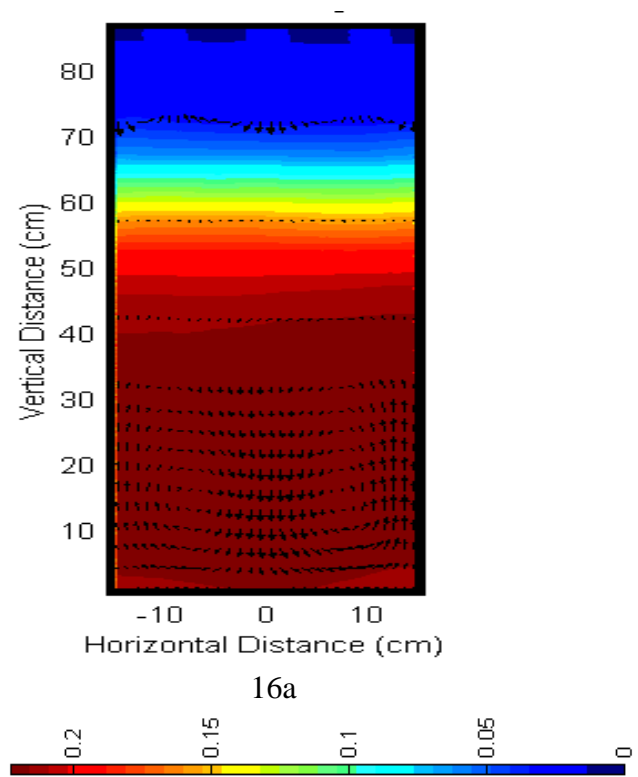


Figure 16. (a) Time-averaged and instantaneous time, (b) 14s (c) 15s (d) 25s (e) 28s volume fraction contour and velocity vector plots for Case FB2 with the corresponding colormap bar for the volume fractions values.

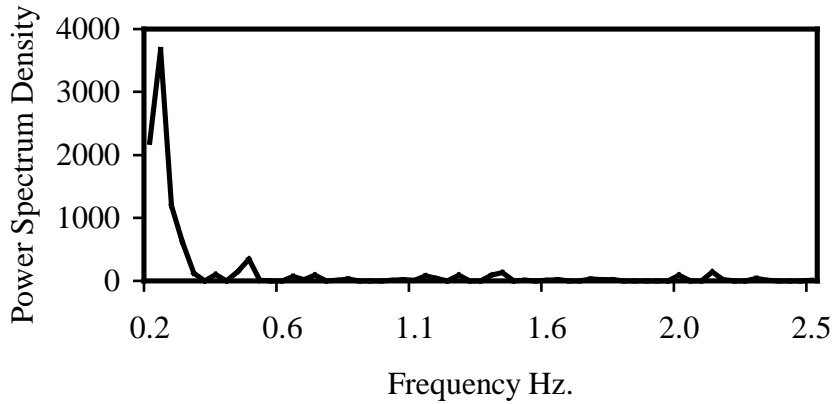


Figure 17. Power Spectrum of the Solid Axial Velocity Profile for Case FB2.

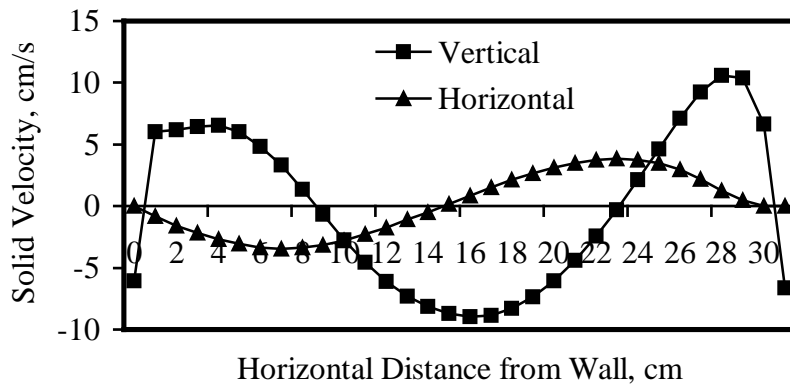


Figure 18. Time-averaged vertical and horizontal particle velocities for Case FB2 at a bed height of 9 cm.

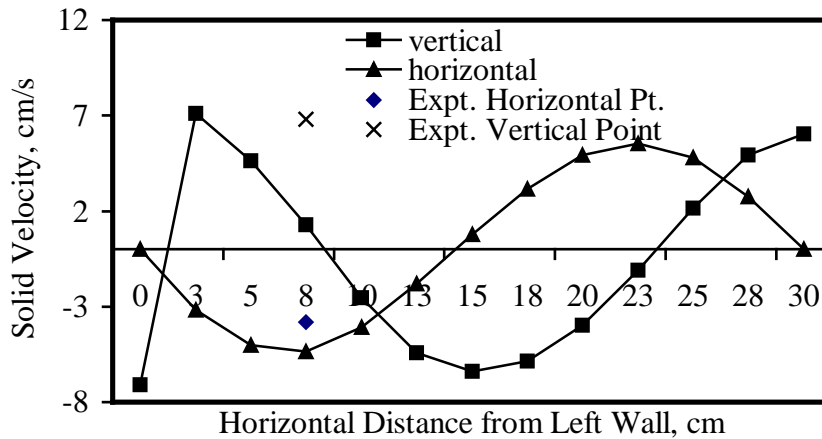


Figure 19. Time-averaged vertical and horizontal particle velocities for Case FB3 at a bed height of 9 cm.

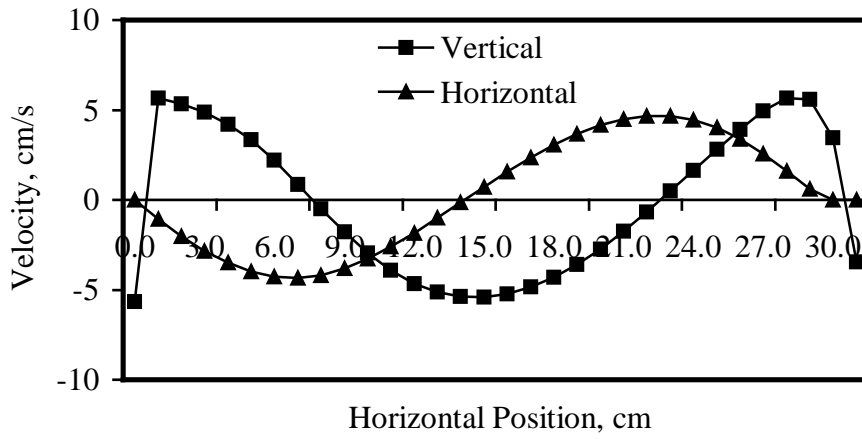


Figure 20. Time-averaged vertical and horizontal particle velocities for Case FB1 at a bed height of 9 cm.

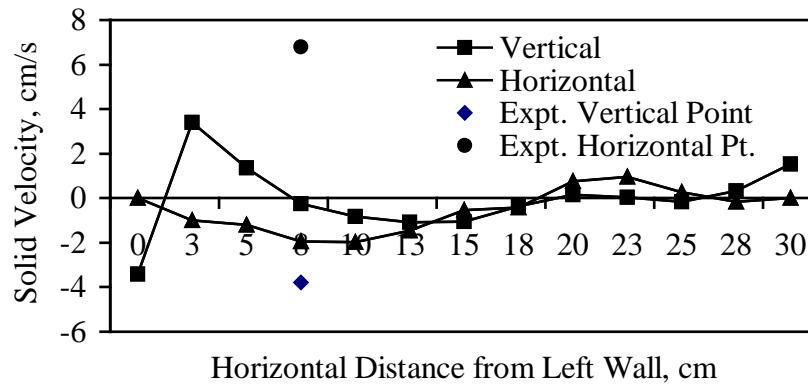


Figure 21. Time-averaged vertical and horizontal particle velocities for Case FB4 at a bed height of 9 cm.

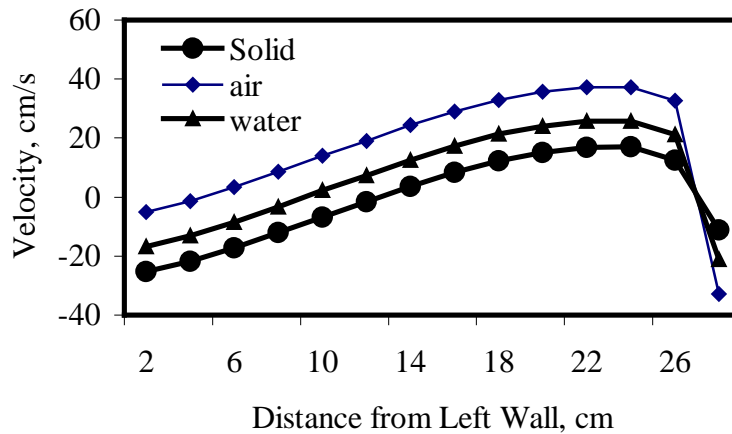


Figure 22. Time-averaged vertical and horizontal particle velocities for Case FB5 at a bed height of 9 cm.

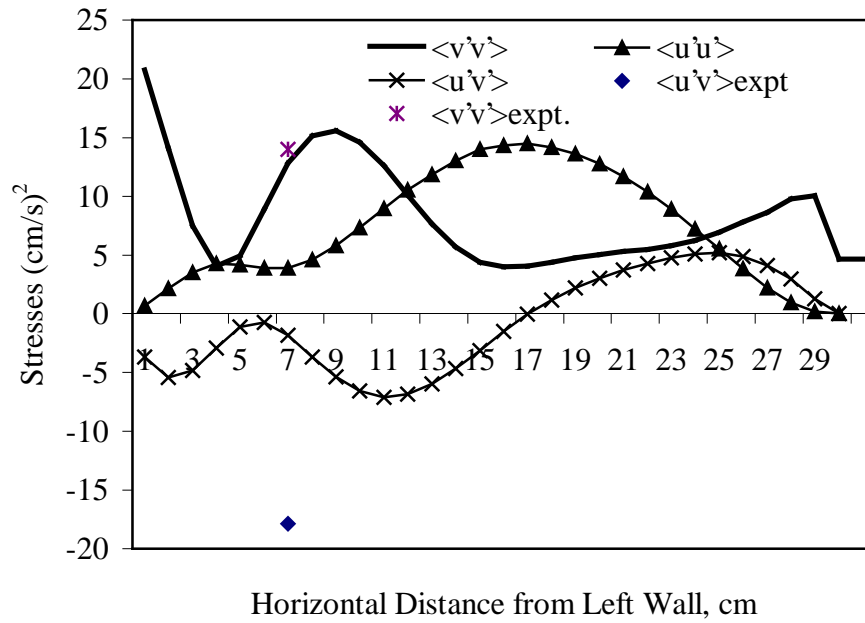


Figure 23. Comparison of computed normal and Reynolds shear stresses for Case FB1 and experimental points at a bed height of 9 cm.

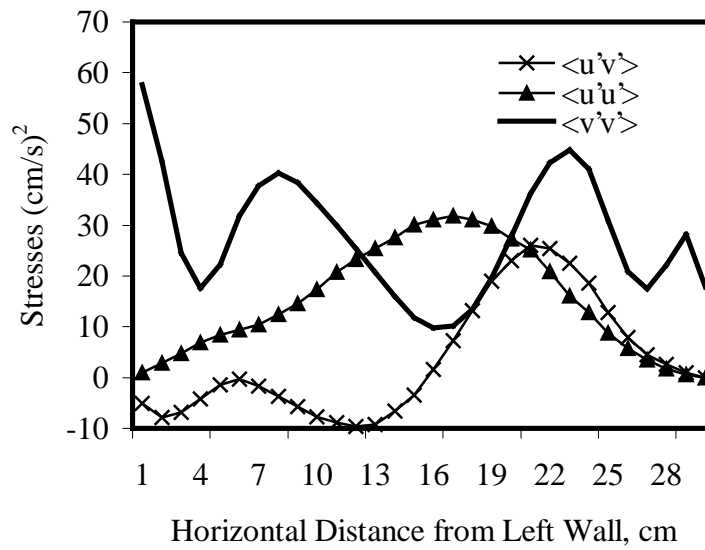


Figure 24. Comparison of computed normal and Reynolds shear stresses for Case FB2 at a bed height of 9 cm.

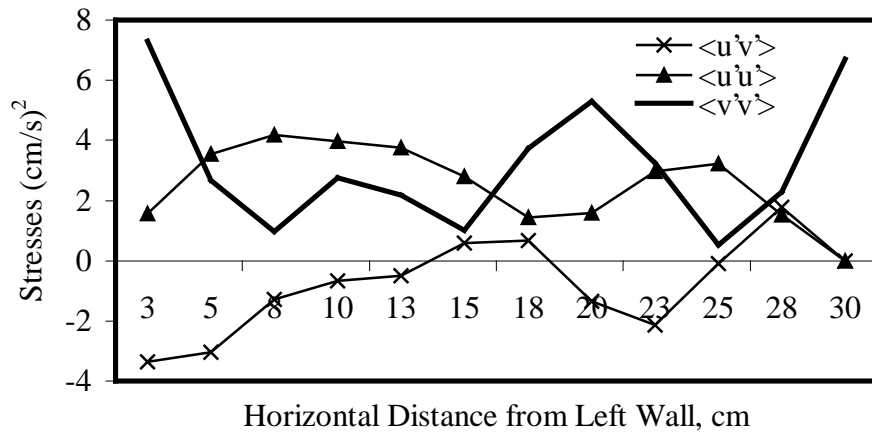


Figure 25. Comparison of computed normal and Reynolds shear stresses for Case FB3 and experimental points at a bed height of 9 cm.

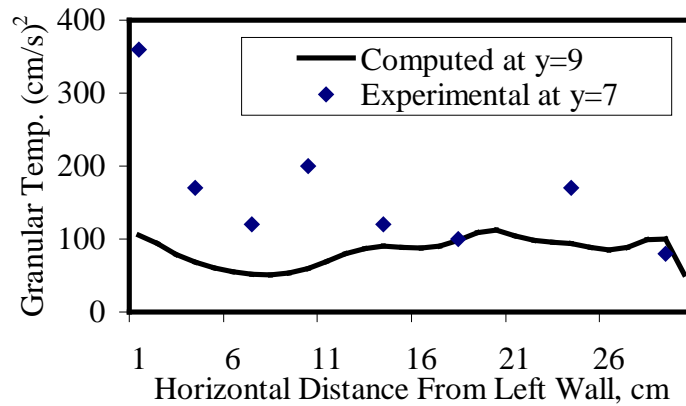


Figure 26. Comparison of computed (Case FB2) and experimental granular temperature points at a bed height of 9 cm.

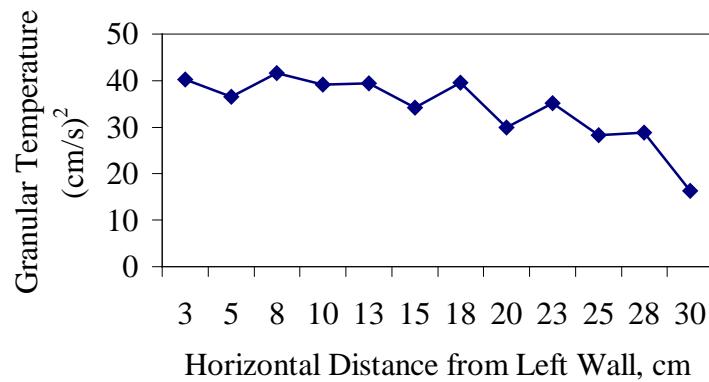


Figure 27. Comparison of computed (Case FB4) granular temperature at a bed height of 9 cm

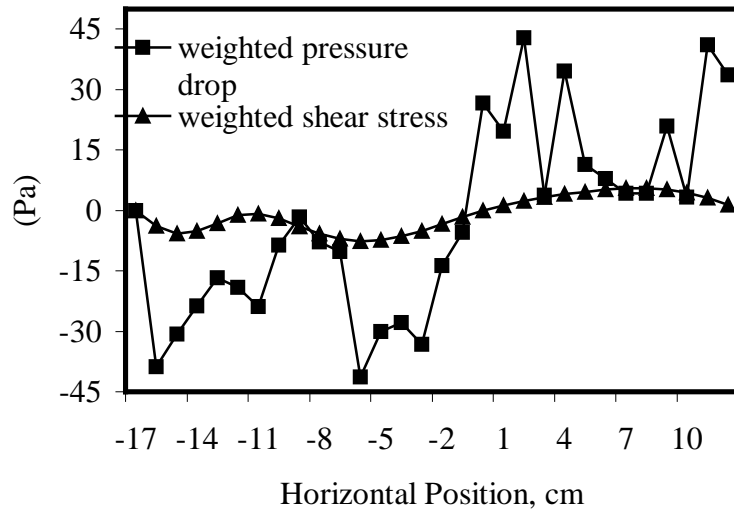


Figure 28. A test for developed flow for case FB3.